

# Turbulent Statistics in a Lubricated Channel Flow



**Alessandro Alati**

Supervisor: Prof. Phil Bowen

Department of Engineering

Cardiff University

This dissertation is submitted for the degree of

*Master of Philosophy*

May 2024



I would like to dedicate this thesis to my family whose support has been invaluable throughout this long journey.



## **Declaration**

This thesis is the result of my own independent work, except where otherwise stated, and the views expressed are my own. Other sources are acknowledged by explicit references. The thesis has not been edited by a third party beyond what is permitted by Cardiff University's Use of Third Party Editors by Research Degree Students Procedure.

### **Statement 1**

This thesis is being submitted in partial fulfilment of the requirements for the degree of MPhil.

### **Statement 2**

This work has not been submitted in substance for any other degree or award at this or any other university or place of learning, nor is it being submitted concurrently for any other degree or award (outside of any formal collaboration agreement between the University and a partner organisation).

### **Statement 3**

I hereby give consent for my thesis, if accepted, to be available in the University's Open Access repository (or, where approved, to be available in the University's library and for inter-library loan), and for the title and summary to be made

available to outside organisations, subject to the expiry of a University-approved bar on access if applicable.

Alessandro Alati

May 2024

## **Acknowledgements**

I am grateful to acknowledge Andrew Crayford for his professionalism and unwavering commitment. His conduct has been a great source of inspiration to me throughout my academic journey and will continue to motivate me in the years to come.



## Abstract

In this work we aim to study, through the use of Direct Numerical Simulations (DNS), the turbulent drag reduction that occurs in a lubricated channel during the transport of a fluid at a low Reynolds number. In this situation, one of the two fluids separates the second from the wall forming a thin layer in contact with it. In our configuration the thin lubricating layer is adjacent to one of the wall, which will be called lubricated side. We consider the same density ( $\rho_1 = \rho_2$ ) for the two fluids, we change the viscosity ratio ( $\lambda = \nu_1/\nu_2$ ) with two different values:  $\lambda = 1$  and  $\lambda = 0.5$ . To assess the role of the surface tension we also performed an additional simulation at  $\lambda = 1$  varying the We number from  $We = 0.055$  to  $We = 0.5$ . As expected the drag reduction (DR) mechanism is strongly related to the viscosity ratio, in particular the flow rate increase when decreasing  $\lambda$  due to a relaminarization of the lubricated layer. Moreover, the parametric analysis on the effect of viscosity ratio and surface tension allows us to highlight very interesting modulations of the dynamics of the interface and of the turbulent kinetic budgets. To date, the latest studies in this area have been carried out using the *Phase Field Method* [1] for the description of the interface. One of the scopes of the present study is to confirm and extend the existing results by exploring the dynamics of the flow with the use of the *Volume of Fluid* (VOF) method [2].



## Publications

Alati, A., De Angelis, E. *Turbulent statistics and interface dynamics in a lubricated channel flow at  $Re_\tau = 100$* . *Meccanica* 58, 1959–1971 (2023). <https://doi.org/10.1007/s11012-023-01697-8>



# Table of contents

<b>Publications</b>	<b>xi</b>
<b>List of figures</b>	<b>xv</b>
<b>List of tables</b>	<b>xix</b>
<b>Nomenclature</b>	<b>xxi</b>
<b>1 Introduction</b>	<b>3</b>
1.1 Turbulent Channel Flow . . . . .	6
1.2 Wall Turbulence . . . . .	7
1.3 Reynolds equations . . . . .	8
1.4 Law of the Wall . . . . .	9
1.5 Mean Velocity Distribution . . . . .	12
1.6 Root Mean Square velocities . . . . .	13
1.7 Direct Numerical Simulation . . . . .	14
1.8 Correlated variables and Intensities . . . . .	16
1.9 Capturing Interface methods . . . . .	16
<b>2 Literature Review</b>	<b>23</b>
2.1 Turbulent Drag Reduction . . . . .	23
2.2 Scale by scale energy budget . . . . .	30
<b>3 Methodology</b>	<b>35</b>
3.1 Volume Of Fluid . . . . .	36

3.2	Incompressible Two-Fluid Flow Solver . . . . .	38
3.3	Simulations set-up . . . . .	41
<b>4</b>	<b>Results</b>	<b>45</b>
4.1	Results and Discussion . . . . .	46
4.2	Probability density functions . . . . .	53
4.3	Turbulent kinetic energy budgets . . . . .	56
4.4	Single point scale energy budget . . . . .	59
4.5	Two point scale energy budget . . . . .	61
<b>5</b>	<b>Conclusions</b>	<b>67</b>
	<b>References</b>	<b>69</b>

# List of figures

1.1	Normalized mean streamwise velocity profile $u^+ = \bar{u}/u_\tau$ plotted against the wall-normal coordinate $z^+ = z u_\tau/\nu$ for single-phase turbulent channel. . . . .	12
1.2	Decomposition of total shear stress in single-phase case. Profiles of the viscous shear stress $\tau_v(z) = \mu d\bar{u}/dz$ (solid line) and the Reynolds shear stress $\tau_t(z) = -\rho \overline{u'w'}$ (dashed line), both normalized by the wall shear stress $\tau_w$ . The sum $\tau_v + \tau_t$ (thin line) is exactly linear in $z$ , balancing the imposed pressure gradient.	14
1.3	Velocity fluctuation intensities in single-phase turbulence. Root-mean-square profiles of the streamwise ( $u_{\text{rms}}$ ), spanwise ( $v_{\text{rms}}$ ) and wall-normal ( $w_{\text{rms}}$ ) velocity fluctuations, normalized by the friction velocity $u_\tau$ . Panel above, the outer coordinate $z/h$ . Panel below, same data in inner units $z^+ = z u_\tau/\nu$ , showing the viscous sublayer ( $z^+ < 10$ ), buffer layer ( $10 < z^+ < 30$ ) and log-law region ( $z^+ > 30$ ). . . . .	15
3.1	Sketch of the computational domain of the channel. . . . .	42
4.1	Cross-section ( $y - z$ ) of the instantaneous streamwise velocity $u$ . In the top left panel the case with $\lambda = 0.5$ . Top right panel refers to the case with $\lambda = 1$ . Bottom panel the case $\lambda = 1$ , $We = 0.5$ . The white line marks the position of the interface. . .	46

- 
- 4.2 Normalized mean streamwise velocity  $\bar{u}^+$  as a function of the wall-normal direction for all the simulated cases. The dotted line at  $z = 1.85$  marks the mean interface position. . . . . 47
- 4.3 Root-mean square velocity fluctuations for single phase and viscosity stratified flows along the  $z$  axis. Streamwise component  $u_{rms}$  left panel above, spanwise component  $v_{rms}$  right panel above, wall-normal component  $w_{rms}$  bottom panel. The dotted line at  $z = 1.85$  marks the mean interface position. . . . . 48
- 4.4 Profile of the viscous shear stress  $\bar{\tau}_v^+$  in the left panel. Turbulent shear stress  $\bar{\tau}_t^+$  and the two contributions together  $\bar{\tau}_v^+ + \bar{\tau}_t^+$ , respectively continuous and dashed line on the right panel. The dotted line at  $z/h = 1.85$  marks the mean interface position. . . 50
- 4.5 Root-mean square vorticity fluctuations for all the simulated cases along the normal axis. Streamwise component  $\omega'_x$  left panel above, spanwise component  $\omega'_y$  right panel, wall-normal component  $\omega'_z$  below. The dotted line at  $z = 1.85$  marks the mean interface position. . . . . 52
- 4.6 Probability Density Function (PDF) of the normalized Wall-Shear stress fluctuations  $\tau'_w = (\tau_w - \bar{\tau}_w)/\bar{\tau}_w$  for all cases. Profiles at the non lubricated wall are on left panel, while the the right panel refers to the lubricated wall. . . . . 53
- 4.7 Probability Density Function (PDF) of the interface elevation  $\eta/h$  at  $\lambda = 1$  with two different Weber number ( $We = 0.055$ ,  $We=0.5$ ) and  $\lambda = 0.5$  with  $We = 0.055$  using a logarithmic scaling. The dotted line at  $z = 1.85$  marks the reference interface position. . . . . 55
- 4.8 Joint Probability Density Function (JPDF) of the normalized Wall-Shear stress fluctuations  $\tau'_w = (\tau_w - \bar{\tau})/\bar{\tau}$  over the interface elevation  $\eta^+$  in viscous units for increasing *Weber* number at  $\lambda = 1$ . . . . . 56

---

4.9	Profiles of the contributions to the TKE budget near the lubricated wall region for the cases $\lambda = 1$ (top left $We = 0.0055$ and right panel $We = 0.5$ , respectively) and for $\lambda = 0.5$ bottom panel.	57
4.10	Budget of turbulent kinetic energy (TKE) vs. wall-normal position $z^+$ in the single-phase channel at $Re_\tau = 100$ . Curves show: (1) production $P(z^+)$ , (2) turbulent transport $T(z^+)$ , (3) viscous diffusion $D(z^+)$ , (4) pressure transport $\Pi(z^+)$ , and (5) dissipation $\varepsilon(z^+)$ . All terms are normalized by $u_\tau^4/h$ . Note how production peaks in the buffer layer ( $5 < z^+ < 30$ ) and is balanced by dissipation in the log layer ( $z^+ > 30$ ), with viscous diffusion dominating very near the wall ( $z^+ < 5$ ).	60
4.11	Energy budget in the viscous sub-layer $z^+ = 4$ , ( $r_x^+ = 1, r_y^+ = 1$ )	63
4.12	Energy budget in the buffer layer $z^+ = 20$ , ( $r_x^+ = 1, r_y^+ = 1$ )	64
4.13	Energy budget in the log-region $z^+ = 50$ , ( $r_x^+ = 1, r_y^+ = 1$ )	64



# List of tables

4.1	Volume flow rate $Q/Q_{SP}$ normalized by the reference Single Phase along with the wall shear stress for the different cases ( <i>SinglePhase</i> ( <i>SP</i> ), $\lambda = 1$ , $\lambda = 0.5$ ) at the bottom wall ( $\bar{\tau}_{w,b}$ ) and top wall ( $\bar{\tau}_{w,t}$ ). . . . .	48
-----	--	----



# Nomenclature

$\bar{u}$	Mean streamwise velocity [m/s]
$\beta$	THINC slope parameter [-]
$\chi$	Interface thickness [m]
$\delta q$	Scale energy [m <sup>2</sup> /s <sup>2</sup> ]
$\delta u'_i$	Velocity increment [m/s]
$\Delta V$	Control volume [m <sup>3</sup> ]
$\delta$	Dirac delta function [1/m]
$\epsilon$	Turbulent dissipation rate [m <sup>2</sup> /s <sup>3</sup> ]
$\epsilon_{ijk}$	Levi-Civita symbol [-]
$\eta$	Interface elevation [m]
$\lambda$	Viscosity ratio ( $\nu_1/\nu_2$ ) [-]
Ch	Cahn number [-]
$\mu$	Dynamic viscosity [Pa · s]
$\mu_c$	Chemical potential [-]
$\nabla$	Gradient operator [1/m]
$\nabla^2$	Laplacian operator [1/m <sup>2</sup> ]

---

$\nu$	Kinematic viscosity [ $\text{m}^2/\text{s}$ ]
$\phi$	Volume of Fluid fraction or Phase-field variable [-]
$\rho$	Density [ $\text{kg}/\text{m}^3$ ]
$\sigma$	Surface tension [ $\text{N}/\text{m}$ ]
$\tau$	Shear stress [ $\text{Pa}$ ]
$\tau_w$	Wall shear stress [ $\text{Pa}$ ]
$f_\sigma$	Surface tension force per unit volume [ $\text{N}/\text{m}^3$ ]
$h$	Channel half-height [ $\text{m}$ ]
$k$	Interface curvature [ $1/\text{m}$ ]
$L$	Reference length [ $\text{m}$ ]
$n$	Unit normal vector [-]
$Pe$	Péclet number [-]
$Q$	Volume flow rate [ $\text{m}^3/\text{s}$ ]
$q$	Turbulent kinetic energy [ $\text{m}^2/\text{s}^2$ ]
$Q_{SP}$	Single-phase volume flow rate [ $\text{m}^3/\text{s}$ ]
$r_i$	Separation vector [ $\text{m}$ ]
$Re$	Reynolds number [-]
$Re_\tau$	Shear Reynolds number [-]
$S_{ij}$	Strain-rate tensor [ $1/\text{s}$ ]
$t$	Time [ $\text{s}$ ]
$T_{ij}$	Viscous stress tensor [ $\text{Pa}$ ]

---

$u$	Streamwise velocity component [m/s]
$u'$	Velocity fluctuation [m/s]
$u^+$	Velocity in viscous units [-]
$u_\tau$	Friction velocity [m/s]
$v$	Spanwise velocity component [m/s]
$w$	Wall-normal velocity component [m/s]
$We$	Weber number [-]
$x$	Streamwise direction [m]
$y$	Spanwise direction [m]
$z$	Wall-normal direction [m]
$z^+$	Wall coordinate in viscous units [-]



**Resumed in parts and based on:**

Alati, A., De Angelis, E. *Turbulent statistics and interface dynamics in a lubricated channel flow at  $Re_\tau = 100$* . *Meccanica* 58, 1959–1971 (2023). Chapter 3 Methodology and 4. Results.



# Chapter 1

## Introduction

Experimentally it has been proved that the presence of lubrication inside a pipeline produces a significant reduction of the wall shear stress, therefore of the energy spent for the transport of the fluid [3-6]. Our current understanding is that this reduction can be mainly explained by the action of viscous forces. Particularly, in the situation in which the lubricated layer has a lower viscosity the resulting increase of the volume flow rate suggests the establishment of a friction loss. When considering a two-phase flow with immiscible fluids we observe a tendency of the less viscous fluid to migrate towards the high shear region. This behavior has allowed an increase of the energy efficiency in the case of transport of viscous fluids in pipeline. In particular the pressure required to sustain the motion is comparable to the scenarios involving only the less viscous fluid. In order to establish this mechanism the viscosity ratio between the two fluids needs to be larger enough, otherwise some instabilities can arise. Other aspects that go beyond the hydrodynamic of the system and therefore will not be taken into account in this study are related to the adherence of the lower viscosity fluid. It has been seen that despite the stability of the flows, the higher viscosity fluid can sometime foul the walls. This aspect represent an important experimental fact that need to be carefully considered in real world application, like the construction of a pipeline. Another insight that require further investigation due to it's effect on the dynamic of the system, is

the ratio between the heights of the two layers. This geometrical component and its optimal value could contribute to complete the understanding of the phenomenon of the drag reduction. Drag Reduction (DR) is the term used in literature to describe the mechanism responsible for the effect of reduced friction at the walls of a channel or a pipeline when to a carrier fluid is added a second fluid on the top in order to create a small film that separate the main one from the walls. The lack of time along with the higher priority in the clarification of the role of the interface, are the main reasons why this study does not contemplate the geometrical discussion. The present study is focused on the analysis of a turbulent channel flow, this refers to a situation in which typically a fluid moves through a rectangular duct. In most of industrial relevant applications we more often find pipelines. This refers to a particular channel in which the shape of the cross section is usually circular. Even though the geometry used in studies (like channels) might differ from actual applications (like pipelines), the underlying physics remains the same. In simulations, due to efficiency, complexity and computational reasons is usually preferred the implementation of simplified geometries. The main phenomena taken into account in this dissertation can be summarised into three categories. Drag reduction, which involves, as already mentioned, all the mechanisms that produce a decrease of resistance as the fluid moves along a channel or a pipe. Near wall dynamic, which explore the fluid behavior at the boundaries. Interface effects, where in multi-phase flows (typically liquid-liquid), examine the the interaction between different phases. All these aspects are crucial in the understanding of the turbulence dynamic and are yet to be fully explained. Moreover none of these depend on the selected geometry, which is why we chose a rectangular duct. The Drag Reduction mechanism responsible for the effect just described has been explored in several directions. As an example, the physics of stratified viscous fluid has been largely investigated through the analysis of the flow instabilities, an extensive review can be found in [36].

In general, the phenomenon has been qualitatively investigated in its global aspects, such as pressure drop and flow rate, but a satisfactory description of flow characteristics has not yet been achieved. This is partly due to experimental limitations and partly to the limited number of Direct Numerical Simulations (DNS) conducted. The latter in particular represents the best tool for the detailed characterization of both phases as well as the evolution of the interface. Some of the most recent studies adopt the Phase Field Method to capture the interface [28, 19, 42]. Ahmadi et al. [19] for instance, considered a turbulent channel flow with two stratified immiscible layers at a shear Reynolds number  $Re_\tau = 100$  with the aim of exploring the dynamic of the interface and how this can affect drag reduction. The choice for the value of the Reynolds shear stress in their work and accordingly, for comparison in this one, mainly depends on the complexity and cost of the simulations performed at higher values. Nevertheless, this value has already overcome the threshold in which all the dynamic structures required for the investigation of the near-wall layers and the interface region are already in place. For the simulation, they used the same density but different viscosity ratio for the two fluids. According to their results, a non-negligible contribution to DR is related to the energy spent to deform the interface, and the effect increases when the viscosity ratio decreases.

In a following study [28] the same authors explored the correlation between the shear stress distribution on the lubricated wall and the elevation of the interface, to confirm the previous observations. In the present study, our aim is to extend these findings by simulating the flow with the Volume of Fluid method. This numerical approach assumes a sharp interface that allows a more realistic description of the interface compared to the Phase Field, which instead considers a continuous variation of the flow properties as a function of an order parameter. The DR is examined here in a channel where a thin layer with equal or lower viscosity is flowing on top of a thicker layer. Specifically, we

selected two values for the viscosity ratio, namely  $\lambda = 0.5$  and  $\lambda = 1$ .

We observed that the DR increases as the viscosity decreases. In particular, when  $\lambda = 0.5$  we see a complete relaminarization of the thin layer. The deformation of the interface and its effect on the DR have been investigated through the variation of the Weber number, which represents the ratio between inertial and cohesive forces. Its value produces a more deformable interface when high, while it is more rigid when low. We observe that when we increase the Weber to  $We = 0.5$  at  $\lambda = 1$  the increase of the DR is slightly larger. We did not find here any appreciable effect related to the capillary forces generated by the surface tension, namely, we do not observe a turbulence reduction due to energy spent in deforming the interface. For all simulations, we adopted  $Re_\tau = 100$ .

The structure of the thesis is as follows. We start below in this chapter with a recap of the main statistics used in the analysis of turbulent flows, the following section covers some aspects of the current approach to the interface capturing methods. The second chapter is a brief literature review about the drag reduction phenomenon and the dynamic of turbulence. In the third chapter, we present the methodology followed in this research, highlighting the methods selected and the differences with respect to previous publications. In the fourth chapter, we discuss the main results we obtained along with statistics that explore and reveal possible mechanisms beyond the phenomenon of the DR. The dissertation ends with the fifth chapter with the conclusions of the work.

## 1.1 Turbulent Channel Flow

A well posed problem is defined by 3 conditions as stated by Hadamard in the 19th century.

1. A solution exists
2. There is only a single solution
3. Small disturbances in the initial or boundary conditions lead only to small variation of the solution.

The first two represent the idea of deterministic behavior. The problem in dealing with real phenomena is that the third condition can only be known with finite accuracy. Navier-Stokes equations are non linear and only in a few cases can satisfy all the well posed conditions, the third in particular. In the other cases, the solution becomes unpredictable. After a certain amount of time, two solutions will begin to diverge completely. For this reason, these phenomena are investigated through statistics methods. Turbulence originates as a consequence of instabilities related to the interaction between viscous and non linear terms. In a turbulent boundary layer, the kinetic energy from the free-stream flow is converted into turbulent fluctuations and then dissipated into internal energy by viscous action [1]. This mechanism is continuous without the presence of stabilizing forces. The complex phenomena of turbulence have been studied taking into account some patterns in the flow that can be observed repeatedly. The idea of coherent motion in this framework refers to a three-dimensional region of the flow over which at least one fundamental flow variable (velocity component, density, temperature, etc.) exhibits significant correlation with itself or with another variable over a range of space and/or time that is significantly larger than the smallest local scales of the flow. Some related processes are the near-wall high and low speed streaks and quasi-streamwise vortices (long, thin tubes of vorticity that are oriented mainly in the streamwise direction).

## 1.2 Wall Turbulence

Considering the Navier-Stokes equations for an incompressible Newtonian fluid

$$\nabla \cdot \mathbf{u} = 0 \quad (1.1)$$

$$\frac{\partial \mathbf{u}}{\partial t} + \mathbf{u} \cdot \nabla \mathbf{u} = -\frac{1}{\rho} \nabla p + \nu \nabla^2 \mathbf{u} \quad (1.2)$$

### 1.3 Reynolds equations

In terms of mean or time-averaged turbulent variables, we write

$$\bar{\mathbf{u}} = \lim_{T \rightarrow \infty} \frac{1}{T} \int_0^T \mathbf{u} dt. \quad (1.3)$$

Reynolds' idea was to split each property into mean plus fluctuating variables

$$\left\{ \begin{array}{l} u(x, y, z, t) = \bar{u}(x, y, z) + u'(x, y, z, t), \\ v(x, y, z, t) = \bar{v}(x, y, z) + v'(x, y, z, t), \\ w(x, y, z, t) = \bar{w}(x, y, z) + w'(x, y, z, t), \\ p(x, y, z, t) = \bar{p}(x, y, z) + p'(x, y, z, t). \end{array} \right.$$

We can rewrite equations (3.1, 3.2) for each component after time averaging.

We get, respectively, the continuity equation.

$$\frac{\partial \bar{u}}{\partial x} + \frac{\partial \bar{v}}{\partial y} + \frac{\partial \bar{w}}{\partial z} = 0, \quad (1.4)$$

The momentum equation in  $x, y, z$  direction

$$\begin{aligned}
\bar{u} \frac{\partial \bar{u}}{\partial x} + \bar{v} \frac{\partial \bar{u}}{\partial y} + \bar{w} \frac{\partial \bar{u}}{\partial z} &= -\frac{\partial \bar{p}}{\partial x} + \frac{\partial}{\partial x} \left( \mu \frac{\partial \bar{u}}{\partial x} - \overline{\rho u'^2} \right) + \\
&\quad \frac{\partial}{\partial y} \left( \mu \frac{\partial \bar{u}}{\partial y} - \overline{\rho u' v'} \right) + \frac{\partial}{\partial z} \left( \mu \frac{\partial \bar{u}}{\partial z} - \overline{\rho u' w'} \right), \\
\bar{u} \frac{\partial \bar{v}}{\partial x} + \bar{v} \frac{\partial \bar{v}}{\partial y} + \bar{w} \frac{\partial \bar{v}}{\partial z} &= -\frac{\partial \bar{p}}{\partial y} + \frac{\partial}{\partial x} \left( \mu \frac{\partial \bar{v}}{\partial x} - \overline{\rho u' v'} \right) + \\
&\quad \frac{\partial}{\partial y} \left( \mu \frac{\partial \bar{v}}{\partial y} - \overline{\rho v'^2} \right) + \frac{\partial}{\partial z} \left( \mu \frac{\partial \bar{v}}{\partial z} - \overline{\rho v' w'} \right), \\
\bar{u} \frac{\partial \bar{w}}{\partial x} + \bar{v} \frac{\partial \bar{w}}{\partial y} + \bar{w} \frac{\partial \bar{w}}{\partial z} &= -\frac{\partial \bar{p}}{\partial z} + \frac{\partial}{\partial x} \left( \mu \frac{\partial \bar{w}}{\partial x} - \overline{\rho u' w'} \right) + \\
&\quad \frac{\partial}{\partial y} \left( \mu \frac{\partial \bar{w}}{\partial y} - \overline{\rho v' w'} \right) + \frac{\partial}{\partial z} \left( \mu \frac{\partial \bar{w}}{\partial z} - \overline{\rho w'^2} \right).
\end{aligned} \tag{1.5}$$

## 1.4 Law of the Wall

We now consider a fully developed region in which the flow is statistically stationary, independent of  $x$  (apart from the pressure) and  $y$ . The velocity statistics only depend on  $z$ . The streamwise ( $x$ ) and the wall-normal ( $z$ ) momentum equation then reduces to ([29])

$$0 = -\frac{\partial \bar{p}}{\partial x} + \frac{d}{dz} \left( \mu \frac{d\bar{u}}{dz} - \overline{\rho u' w'} \right), \tag{1.6}$$

$$0 = -\frac{\partial \bar{p}}{\partial z} - \frac{d}{dz} \left( \overline{\rho w'^2} \right). \tag{1.7}$$

Integrating equation (1.7) we obtain

$$p(x, z) = -\overline{\rho w'^2} + p_w. \tag{1.8}$$

Inserting in (1.6) and considering the term  $d\overline{\rho w'^2}/dz = 0$  since the constant value of the pressure gradient in the wall-normal direction which leads to zero the first term on the right-hand side of equation (1.7) results in the following.

$$0 = - \int \frac{\partial p_w}{\partial x} dz + \frac{d}{dz} \left( \mu \frac{d\bar{u}}{dz} - \int \overline{\rho u' w'} \right) dz, \quad (1.9)$$

$$0 = - \frac{\partial p_w}{\partial x} z + \mu \frac{d\bar{u}}{dz} - \overline{\rho u' w'} - \tau_w. \quad (1.10)$$

In the half-channel (symbol  $h$ ) the contribution of total stress is zero, leading to

$$\frac{\partial p_w}{\partial x} = - \frac{1}{h} \tau_w. \quad (1.11)$$

The two contributions of the total stress decrease linearly along the channel, so we can write

$$\mu \frac{d\bar{u}}{dz} - \overline{\rho u' w'} = \left( 1 - \frac{z}{h} \right) \tau_w. \quad (1.12)$$

In what follows, the Prandtl approach [3], has been considered because even if it turned out to be inaccurate, it maintains a strong physical intuition. Prandtl, in order to evaluate the turbulent stress, assumed the proportionality of this with  $d\bar{u}/dz$  through a quantity he called mixing length  $L$

$$\tau = \mu \frac{d\bar{u}}{dz} + \rho L^2 \left( \frac{d\bar{u}}{dz} \right)^2. \quad (1.13)$$

One can notice that the kinetic energy of the turbulent fluctuation is absorbed approaching the wall, and as a consequence the mixing length becomes zero. Prandtl suggested that the simplest way to quantify the mixing length was therefore the relation  $L = kz$ , where  $k$  is called the van Karman constant [4]. He also assumed that the Reynolds stress at the wall is constant and takes the form

$$\tau_w = \rho k^2 z^2 \left( \frac{d\bar{u}}{dz} \right)^2. \quad (1.14)$$

Manipulating the latter equation, we can write

$$\frac{d\bar{u}}{dz} = \frac{\sqrt{\tau_w/\rho}}{kz}. \quad (1.15)$$

Since the term  $\sqrt{\tau_w/\rho}$  has the dimensions of velocity, it has been called *Friction Velocity*  $u_\tau$ . Substituting this term, the equation becomes

$$\frac{d\bar{u}}{u_\tau} = \frac{1}{k} \frac{dz}{z}. \quad (1.16)$$

The integral of the previous equation is called *Law of the Wall*. After the integration we obtain

$$\frac{\bar{u}}{u_\tau} = \frac{1}{k} \ln(z) + C. \quad (1.17)$$

where  $C$  and  $k$  are two experimental constants. It is evident that when  $z \rightarrow 0$ ,  $\bar{u} \rightarrow -\infty$ . We can define  $z_0$  as the distance where  $\bar{u}$  becomes zero, and in this way we can evaluate the constant  $C$  as

$$C = -\frac{1}{k} \ln\left(\frac{z}{z_0}\right). \quad (1.18)$$

Inserting this into equation (1.16) yields

$$\frac{\bar{u}}{u_\tau} = \frac{1}{k} \ln\left(\frac{z}{z_0}\right). \quad (1.19)$$

Prandtl guessed that  $z_0$ , which has dimensions of a length, had to be proportional to  $\nu/u_\tau$

$$z_0 = \beta \frac{\nu}{u_\tau}. \quad (1.20)$$

Substituting the relation gives

$$\frac{\bar{u}}{u_\tau} = \frac{1}{k} \ln\left(\frac{zu_\tau}{\nu\beta}\right), \quad (1.21)$$

$$\frac{\bar{u}}{u_\tau} = \frac{1}{k} \left[ \ln\left(\frac{zu_\tau}{\nu}\right) - \ln(\beta) \right]. \quad (1.22)$$

Experimental measurements lead to  $k = 0.41$ ,  $\beta = 0.111$ . The values for these constants are universal in wall-bounded turbulence and were derived with accurate empirical measurements. In this way, the previous equation can be written as

$$\frac{\bar{u}}{u_\tau} = 2.5 \ln\left(\frac{zu_\tau}{\nu}\right) + 5.5. \quad (1.23)$$

The two normalizations of the quantity  $\bar{u}/u_\tau$  and  $zu_\tau/\nu$  can be respectively defined as  $u^+$ ,  $z^+$ . The superscript  $+$  indicates the non-dimensional quantity scaled by the wall variables and takes the name of wall unit.

$$\bar{u}^+ = 2.5 \ln(z^+) + 5.5. \quad (1.24)$$

This equation is valid only in the region where the viscous effects are negligible, approaching the wall we can find deviation from this law, where turbulent stress decreases to zero.

## 1.5 Mean Velocity Distribution

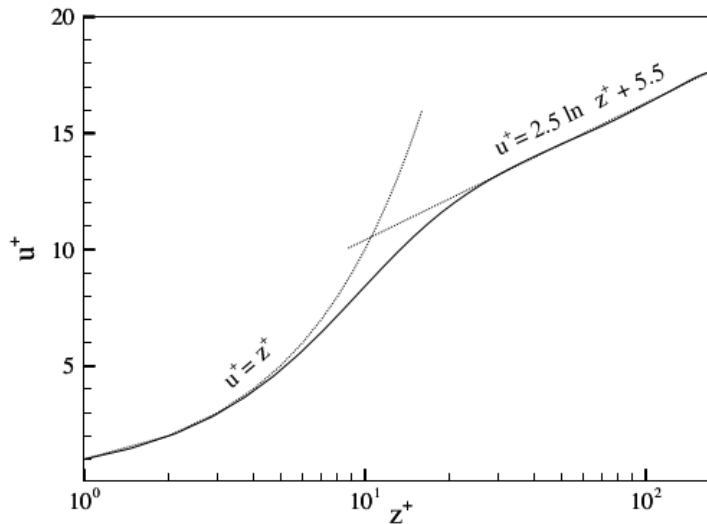


Fig. 1.1 Normalized mean streamwise velocity profile  $u^+ = \bar{u}/u_\tau$  plotted against the wall-normal coordinate  $z^+ = zu_\tau/\nu$  for single-phase turbulent channel.

The near-wall can region be sub-divided into three different areas.

- viscous sub-layer  $0 < z^+ < 10$
- buffer layer  $10 < z^+ < 30$
- log-law region  $z^+ > 30$

Viscous shear is dominant near the wall, where the effects of turbulence are negligible. The opposite situation occurs in the outer region, while in the buffer layer both effects have importance, as we can see in fig.(1.1). Scaling equation (1.12) with the wall variables, we obtain the relation

$$\frac{d\overline{u^+}}{dz^+} - \frac{\overline{u'w'}}{u_\tau^2} = 1 - \frac{z^+}{Re_\tau}. \quad (1.25)$$

In which  $Re_\tau = u_\tau h/\nu$ .

## 1.6 Root Mean Square velocities

Before approaching the statistics and results of the two-phase problem, it is useful to recall the canonical statistics of the single-phase turbulent channel flow. In literature it is customary to use the standard deviation of the velocity fluctuations, namely the root mean square of the velocities, usually these quantities are normalized by the wall-shear velocity  $u_\tau$ .

$$u_{rms} = \sqrt{\frac{1}{N} \sum_{i=1}^N u_i'^2} \quad (1.26)$$

Figure 1.2 shows how the total shear stress decomposes into viscous and Reynolds contributions across the channel. Figure 1.3 then presents the root-mean-square intensities of the three velocity components, highlighting the viscous sublayer, buffer layer and outer region structure. In Chapter 4 we will use these trend as reference when evaluating the drag reduction in the lubricated cases.

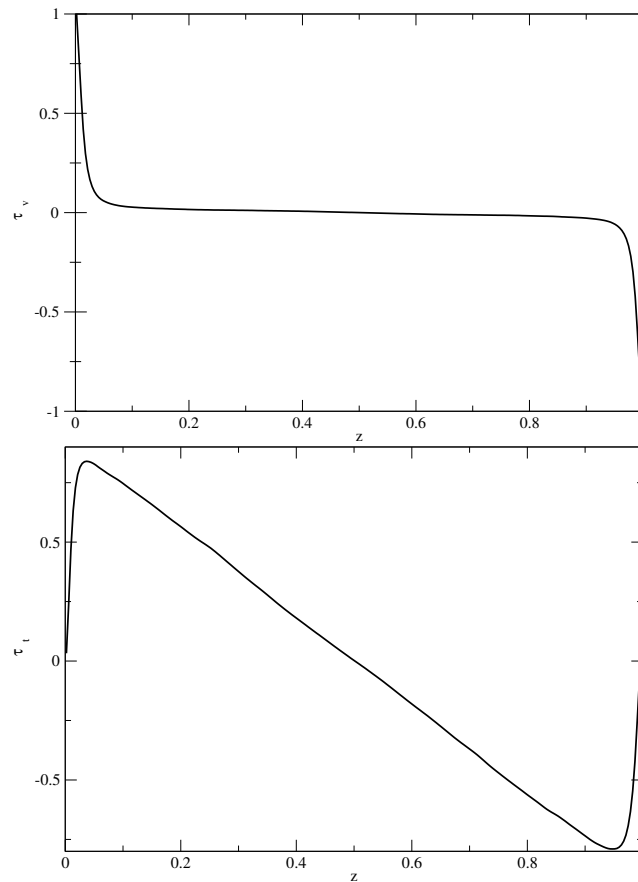


Fig. 1.2 Decomposition of total shear stress in single-phase case. Profiles of the viscous shear stress  $\tau_v(z) = \mu d\bar{u}/dz$  (solid line) and the Reynolds shear stress  $\tau_t(z) = -\rho \overline{u'w'}$  (dashed line), both normalized by the wall shear stress  $\tau_w$ . The sum  $\tau_v + \tau_t$  (thin line) is exactly linear in  $z$ , balancing the imposed pressure gradient.

## 1.7 Direct Numerical Simulation

The mean equations (1.5) have been derived without any approximations. However, these contain additional unknowns compared to the previous situation, namely the Reynold stresses. These quantities take the form of correlations between fluctuations terms. A system with more unknown than equations is called unclosed and can not be solved. A possible solution is the derivation of a second order equation for the evolution of the stresses, but unfortunately such equation contain new third order terms. Proceeding in this way, the closure is never achieved, at one point it is necessary to introduce approximation. Several models have been derived in this view. Direct Numerical Simulation consists on

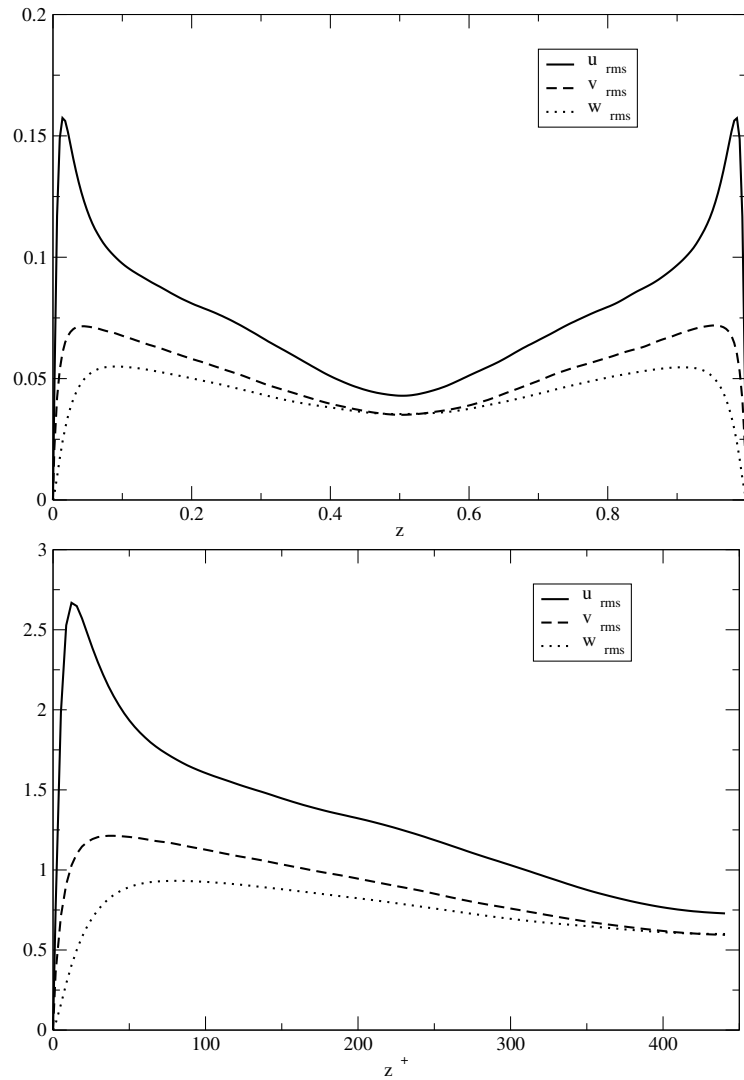


Fig. 1.3 Velocity fluctuation intensities in single-phase turbulence. Root-mean-square profiles of the streamwise ( $u_{\text{rms}}$ ), spanwise ( $v_{\text{rms}}$ ) and wall-normal ( $w_{\text{rms}}$ ) velocity fluctuations, normalized by the friction velocity  $u_\tau$ . Panel above, the outer coordinate  $z/h$ . Panel below, same data in inner units  $z^+ = z u_\tau / \nu$ , showing the viscous sublayer ( $z^+ < 10$ ), buffer layer ( $10 < z^+ < 30$ ) and log-law region ( $z^+ > 30$ ).

solving the Navier-Stokes equations without any added model and represents the most accurate and conceptually simple approach. Unfortunately, its cost most of the time is computationally prohibitive.

## 1.8 Correlated variables and Intensities

If  $\overline{u_i' u_j'} \neq 0$  the two quantities are said to be *correlated*, if  $\overline{u_i' u_j'} = 0$  they are *uncorrelated*. When two fluctuating variables  $a, b$  have the same sign most of the time, this makes  $\overline{ab} > 0$ . A measure of the degree of correlation between two variables  $\overline{u_i'}$  and  $\overline{u_j'}$  is obtained by dividing  $\overline{u_i' u_j'}$  by the square root of the product of the variances; this gives a correlation coefficient, defined as

$$c_{ij} = \frac{\overline{u_i' u_j'}}{\sqrt{\overline{u_i'^2} \overline{u_j'^2}}}. \quad (1.27)$$

After the mean value one of the most important quantity in statistics of turbulence is the variance,

$$\sigma(x)^2 = \overline{(x - \bar{x})^2}. \quad (1.28)$$

This measure is an estimate of width of the variations compared to the average. In turbulence, we use the root mean square of the velocity fluctuation, as its name suggests it gives an idea of the intensity of the turbulence.

## 1.9 Capturing Interface methods

Two-phase flows are central to a wide range of natural and industrial processes, from rain formation and breaking waves to spray atomization and bubbly flows. This paragraph reports a comprehensive survey of interface-capturing methods used in two-phase flow simulations of present times [42]. We also discuss enduring challenges in two-phase flow modeling, highlighting the advantages and disadvantages of different interface-capturing techniques. We will eventually need to survey this expanding literature but will only concentrate on methods known to have been used or currently under development due to limitations in space. For each category, we go through the category over time, tracking the important milestones, state-of-the-art, and promising directions. Multiphase flows encompass a broader spectrum and, not least in including problems

with two fluid phases, constitute one special sub-discipline of computational fluid dynamics. This review is restricted to immiscible two-phase flows only. Theoretical studies of such flows go back to the 19th century (e.g. Plateau, 1873), however, there are only few cases for which the analytical solution is possible even for the easiest problems. Experimental observations are also difficult to carry out for two-phase flows because of their complex behavior [11]. It is obvious that the implementation of numerical approaches that allow for the representation of the free-surface and its coupling with the momentum conservation equation still requires the solution of accurate, physically-sound, low computational-cost equations. Creating such methods is hard because of a number of challenges, such as:

- Applying conservation of mass, momentum and kinetic energy
- Treating large density jumps or property discontinuities across the interface.
- Works with complex topologies and scale separations.
- Correct implementation of the surface tension forces

Interface-capturing procedures are tied to the momentum equation by the calculation of local density, viscosity and surface tension forces. We will mainly compare two different approaches for tracking the interface, a sharp-interface evaluation, such as the Volume of Fluid and diffuse-interface methods, like the Phase Field, where the phase is modeled by an indicator function. Surface tension forces can be applied as stresses or body forces, denoted as integral and volumetric formulations. A discrete balance of surface tension and pressure gradient terms is a crucial requirement for two-phase flow solvers. Although the momentum-conservation property is satisfied by the automatic conservation provided by an integral formulation, the required balance is hard to attain. On the other hand, volumetric formulations have been more successful in achieving this goal and hence have been more prevalent in the literature. The momentum equations in non-conservative and conservative forms are expressed as:

$$\frac{\partial \mathbf{u}}{\partial t} + \nabla \cdot (\mathbf{u} \otimes \mathbf{u}) = \frac{1}{\rho} \left[ -\nabla P + \nabla \cdot (\mu(\nabla \mathbf{u} + \nabla \mathbf{u}^T)) + \mathbf{F}_{ST} \right]$$

$$\frac{\partial(\rho \mathbf{u})}{\partial t} + \nabla \cdot (\rho \mathbf{u} \otimes \mathbf{u}) = -\nabla P + \nabla \cdot (\mu(\nabla \mathbf{u} + \nabla \mathbf{u}^T)) + \mathbf{F}_{ST}$$

where  $\mathbf{F}_{ST}$  denotes the surface tension force. Ensuring accurate computation of the normal vector ( $\mathbf{n}$ ) and curvature ( $\kappa$ ) is essential for different surface tension calculation methods. A common approach involves computing normal vectors by differentiating a smooth field and obtaining curvatures through divergence of these normals. In sharp-interface approaches like VOF, height-functions have been used for more accurate estimation, though their accuracy diminishes at low resolutions.

**The Volume of Fluid Method** has been developed for locating and advecting a fluid interface. This method can be described introducing a *Color Function*  $H(\mathbf{x}, t)$  such that  $H(\mathbf{x}, t) = 1$  in the presence of a fluid or  $H(\mathbf{x}, t) = 0$ . As the fluid moves due to the velocity flow, the color function is updated by the advection equation

$$\frac{\partial H}{\partial t} + \mathbf{u} \cdot \nabla H = 0. \quad (1.29)$$

The volume fraction of the Volume of Fluid can be defined as

$$\phi(\mathbf{x}, t) = \frac{1}{V_0} \int_V H(\mathbf{x}, t) dV', \quad (1.30)$$

where  $V_0$  is the volume of a specific cell.

**Geometric VOF** methods reconstruct the interface within each computational cell and then advect it. The Piecewise-Linear Interface Calculation Scheme (PLIC) [12] is widely used, where the interface is approximated by a line or a plane:

$$\mathbf{n} \cdot \mathbf{x} + \alpha = 0,$$

with  $\alpha$  chosen to enforce that the cut volume equals  $C_k$ . The interface normal  $\mathbf{n}$  can be computed using methods like the Youngs' method or the mixed Youngs-centered (MYC) method.

**Algebraic VOF (AVOF)** methods approximate the phase indicator function  $H$  using numerical methods, classifiable into compressive and THINC schemes. Compressive schemes compute fluxes based on interface orientation, while THINC schemes assume a hyperbolic-tangent profile for  $H$ , providing an accuracy comparable to geometric VOF at a lower cost.

**Level-set methods** initially developed for image processing, were adapted for two-phase flows by Sussman et al. [13]. The level-set function  $\phi(\mathbf{x}, t)$  represents the signed distance to the interface, evolving according to:

$$\frac{\partial \phi}{\partial t} + \mathbf{u} \cdot \nabla \phi = 0.$$

Reinitialization restores the signed-distance property of  $\phi$ , essential for accurate normal and curvature calculations. However, mass conservation remains a significant challenge, mitigated by various correction methods like hybrid particle level set (HPLS) [14] and adaptive mesh refinement (AMR) [15].

**Conservative Level-set methods.** To address the issue of mass conservation while keeping the advantages, a *conservative level-set* (CLS) method was proposed by Olsson Kreiss [16]. The idea is that rather than advecting a signed distance function, CLS evolves an order-parameter  $\phi \in [0, 1]$  with a diffuse-interface profile

$$\phi(\mathbf{x}) = \frac{1}{2} \left[ 1 + \tanh\left(s(\mathbf{x})/(2\varepsilon)\right) \right],$$

where  $s(\mathbf{x})$  is the signed distance and  $\varepsilon$  the interfacial thickness. In each time step  $\phi$  is first advected in conservative, then reinitialized in pseudo-time via

$$\frac{\partial \phi}{\partial \tau} = \nabla \cdot [\varepsilon \nabla \phi - \phi(1 - \phi) \mathbf{n}],$$

with  $\mathbf{n} = \nabla \phi / |\nabla \phi|$ . This two-step algorithm exactly conserves the total volume and allows a straightforward computation of normals and curvature directly from  $\phi$ .

**Phase-field methods** modify the transport equation to account for the physical effects governing thin interfaces. These methods use the Cahn-Hilliard or Allen-Cahn equations derived from the Ginzburg-Landau-Wilson free energy functional. The Cahn-Hilliard equation conserves total mass and is more popular in two-phase flow modeling:

$$\frac{\partial \phi}{\partial t} + \nabla \cdot (\mathbf{u}\phi) = -\nabla^2 [\varepsilon^2 \nabla^2 \phi - W'(\phi)],$$

where  $\phi$  varies between -1 and 1 representing the two phases. Despite advantages in robustness and stability, phase-field methods often require handling fourth-order spatial derivatives and suffer from artificial energy dissipation.

**Hybrid methods**, such as CLSVOF [5] and front-tracking coupled with VOF [6], aim to combine the strengths of different approaches. CLSVOF, for example, leverages the accurate normal and curvature calculations of level-sets with the mass conservation of VOF. These methods, while accurate, face challenges in parallel scalability and computational cost.

The most significant challenge remains the development of methods that efficiently conserve mass, momentum, and total energy. VOF and phase-field methods show the most promise for future research and practical applications. In addition, standardized benchmarks and test cases to evaluate new methods

in realistic conditions. Further research into multi-physics aspects, such as electrostatic and acoustic interactions, is also crucial for advancing the field.



# Chapter 2

## Literature Review

### 2.1 Turbulent Drag Reduction

The study of immiscible two-phase flows, especially within confined geometries, has profound implications in various industrial applications such as petroleum transport and chemical processing. The paper by Ahmadi et al. [19] delves into the dynamics of turbulent Poiseuille flow involving viscosity-stratified fluids. The primary objective is to explain how the varying viscosity ratios between two immiscible liquid layers affect turbulent drag and flow characteristics within a rectangular channel. The authors employed Direct Numerical Simulation (DNS) to investigate the complex interactions between two liquid layers of differing viscosities. The computational setup consisted of a thin upper layer (fluid 1) and a thicker lower layer (fluid 2) with a thickness ratio  $h_1/h_2 = 1/9$ . Both fluids had identical densities, thus negating buoyancy effects, but differing viscosities with three viscosity ratios  $\lambda = \nu_1/\nu_2$  being examined:  $\lambda = 1$ ,  $\lambda = 0.875$ , and  $\lambda = 0.75$ .

The simulations utilized a Phase Field method, governed by the Cahn-Hilliard equation, to accurately capture the interface dynamics. The governing equations included the continuity equation, the Navier-Stokes equations for momentum conservation, and the Cahn-Hilliard equation for the order parameter  $\phi$ , which differentiates the two phases. The dimensionless form of the governing equations

was:

$$\begin{aligned}\nabla \cdot \mathbf{u} &= 0, \\ \frac{\partial \mathbf{u}}{\partial t} + \mathbf{u} \cdot \nabla \mathbf{u} &= -\nabla \tilde{p} + \frac{1}{Re_\tau} \nabla^2 \mathbf{u} + \nabla \cdot \left[ k(\phi, \lambda) (\nabla \mathbf{u} + \nabla \mathbf{u}^T) \right] + \frac{3\sqrt{8}}{WeCh} \mu \nabla \phi, \\ \frac{\partial \phi}{\partial t} &= -\mathbf{u} \cdot \nabla \phi + \frac{1}{Pe} \nabla^2 \mu,\end{aligned}$$

where  $\mu$  is the chemical potential derived from the free energy functional  $F(\phi)$ :

$$\begin{aligned}F(\phi) &= f_0(\phi) + \frac{1}{2} Ch^2 |\nabla \phi|^2, \\ \mu &= \frac{\delta F}{\delta \phi} = \phi^3 - \phi - Ch^2 \nabla^2 \phi.\end{aligned}$$

Viscosity was modeled as a linear function of  $\phi$ :

$$\nu(\phi) = \nu_1 \frac{1 + \phi}{2} + \nu_2 \frac{1 - \phi}{2},$$

recast in terms of the viscosity ratio  $\lambda$ :

$$k(\phi, \lambda) = \nu_2 + \nu_2(\lambda - 1) \frac{\phi + 1}{2}.$$

The order parameter  $\phi$  takes opposite values depending on the phase considered, typically  $-1$  and  $1$ , while varying between these in the interval. The simulations were conducted in a computational domain of dimensions  $4\pi h \times 2\pi h \times 2h$ , discretized with  $512 \times 256 \times 257$  grid nodes. Periodic boundary conditions were applied along the streamwise and spanwise directions, with no-slip conditions at the walls. The time integration employed an implicit Crank-Nicolson scheme for the diffusive terms and an explicit Adams-Bashforth scheme for the nonlinear terms. The simulations revealed significant modulation of turbulence as a result of the presence of the liquid-liquid interface. The volume flow rate, normalized by the single-phase flow rate  $Q_{SP}$ , increased with decreasing  $\lambda$ . This was attributed to the reduction in the wall-normal momentum transport caused by the deformable interface, which converted the mean kinetic energy into the potential energy. The streamwise velocity

profile exhibited an inflection point at the interface, indicative of the shear exerted by the layers. Further analysis of velocity fluctuations showed that near-wall turbulence was slightly enhanced near the bottom wall but significantly suppressed near the top wall. This suppression was more pronounced for lower  $\lambda$  values, as the lower viscosity of fluid 1 facilitated easier deformation of the interface. The spanwise vorticity profiles indicated the presence of counter-rotating rolls at the interface, with their strength diminishing with lower  $\lambda$ . In their work Ahmadi demonstrated that viscosity stratification in two-phase channel flows can effectively reduce turbulent drag, primarily by altering the momentum transport and inducing significant changes in flow dynamics.

In the paper Near Wall Surface Tension Active Interface [28] The authors developed an earlier study to investigate the resonance suppression of turbulence within a viscosity-stratified two-phase flow, with Direct Numerical Simulation (DNS) and Phase Field Method (PFM). The paper studies the behavior of immiscible fluid layers in flow driven by an imposed pressure gradient providing insight into the manner in which changes in viscosity ratios may affect turbulence and wall shear stress in a rectangular channel. Ahmadi et al., utilized DNS combined with PFM to examine the interfacial processes between two immiscible fluid layers. The computational setup is a two-layer configuration which contains a thin upper layer (fluid 1) and a thicker heavy lower layer (fluid 2) with a depth thickness ratio  $h_2/h_1 = 9$ . The buoyancy effects have been removed by setting the densities of the two layers to be the same, but their viscosity has been differentiated with three viscosity ratios  $\lambda = 1$ ,  $\lambda = 0.875$ , and  $\lambda = 0.75$ . The simulations were performed in a periodic domain  $L_x \times L_y \times L_z = 4\pi h \times 2\pi h \times 2h$  grid points as before. No-slip conditions were implemented at the walls, and streamwise as well as spanwise periodic boundary conditions were applied. Time integration used an IMEX scheme, blending implicit for the linear terms and explicit for the non-linear terms. The simulation was initialized from a homogenized single-phase turbulent flow at  $Re_\tau = 100$

that gradually morphed into a two-phase regime. The liquid-liquid interface surprisingly induced some remarkable turbulence modulation, especially close to the liquid-liquid interface and the top wall. This reduction in wall-shear stress and turbulence suppression extended beyond the immediate vicinity of the interface, demonstrating the significant impact that the presence of the interface had on flow dynamics. They showed that the liquid-liquid interface has a large impact on the mean flow behavior. They found a remarkable augmentation in volume flow rate, which is the result of the conversion of the mean kinetic energy to the ionization energy of a deformed interface and this is the novelty with respect to their previous work. A particular focus of the study was the wall shear stress inversions and local recirculation regions that were generated due to the transmission line and interface dynamics, that highlighted the intricate oscillations between interface and near-wall turbulence.

In the paper Turbulent Drag Reduction by Compliant Lubricating Layer by Roccon et al. (2021) [35] the setup considered in the previous studies only differs for the extension of the  $\mathfrak{R}_{\tau_{au}}$  number, here equal to 300. The authors focus on a channel configuration characterized by two usual 2 fluid layers driven by an imposed pressure gradient. The thin lubricating layer is here  $0.15h$  thick and a thicker main fluid layer  $1.85h$  thick), where  $h$  denotes the half-channel height. The 2 fluids have different viscosities  $\eta_1$  and  $\eta_2$ , but same density. The study employs a Phase Field Method to model the liquid-liquid interface, characterized by a uniform surface tension  $\sigma$ . The simulations confirmed again that drag reduction is deeply influenced by the viscosity ratio  $\lambda$ . The volume flow rates for both layers  $(Q_1, Q_2)$  increased relative to the single-phase case  $(Q_{sp})$ , indicating the drag reduction mechanism. It is important to notice that the maximum value for the drag reduction was observed for  $\lambda = 1$ , corresponding to a complete relaminarization of the lubricating layer, while a smaller decrease in drag reduction was observed for lower  $\lambda$  values. The total

shear stress ( $\tau_{tot}$ ) in the wall-normal direction  $z/h$  was decomposed into viscous shear stress ( $\tau_v$ ), turbulent shear stress ( $\tau_t$ ), and capillary stress ( $\tau_c$ ):

$$\tau_{tot} = \langle \eta(z) \rangle \frac{1}{Re_\tau} \frac{\partial \langle u_x \rangle}{\partial z} + \langle u'_x u'_z \rangle + \frac{3\sqrt{8}Ch}{We} \left\langle \frac{\partial \phi}{\partial x} \frac{\partial \phi}{\partial z} \right\rangle.$$

In the analysis, it is reported that for  $\lambda = 1$ , the viscous shear stress near the interface presents a quasi-linear profile, typical of laminar flows. For  $\lambda = 0.25$ , the turbulent stress was higher, suggesting a strong turbulence in the lubricating layer. The capillary stress, essential for drag reduction, was significant in decoupling the main and lubricating layers dynamics, with its effects varying based on the viscosity ratio. The PDFs of the normalized wall shear stress fluctuations ( $\tau'_w$ ) provided further insights into drag reduction mechanisms. For  $\lambda = 1$ , the PDFs at the top wall were nearly symmetric and peaked around zero, reflecting reduced shear stress fluctuations and relaminarization. For  $\lambda = 0.25$ , the PDFs were positively skewed, indicating sustained turbulence and higher wall shear stress fluctuations. Overall, the study highlighted the critical role of surface tension along with the viscosity ratio. The research identifies two distinct DR mechanisms: A surface-tension-driven relaminarization for  $\lambda = 1$  and a viscosity-driven turbulence reduction for smaller value of  $\lambda$ . The results revealed the complex interaction between viscous, inertial, and capillary forces.

In the second paper by Roccon et al. (2021) [36] five different viscosity ratios were considered to capture a wide range of cases from 0.25 to 4. DNS was performed under the constant power input (CPI) method, which keeps injecting constant power into the flow and changes the flow rate corresponding to the local pressure gradients at every moment. Phase Field Method (PFM) was again employed to describe the liquid-liquid interface dynamics. The simulations were conducted in a computational domain of  $4\pi h \times 2\pi h \times 2h$ , with  $512 \times 256 \times 257$  grid points for single-phase cases and  $1024 \times 512 \times 513$  for two-phase simulations, ensuring high-resolution capture of interface dynamics and turbulence structures. The study reveals that a significant drag reduction can

be achieved for  $\lambda \leq 2.00$ . Interestingly, drag reduction does not monotonically correlate with the viscosity ratio. The maximum drag reduction was observed at  $\lambda = 1.00$ , where the flow rate increased by approximately 13%. This behavior is attributed to two distinct drag reduction mechanisms identified through detailed energy budget analysis. For  $\lambda = 1.00$  and  $\lambda = 2.00$ , drag reduction is predominantly due to surface tension effects, which act as an elasticity element separating the two fluids. This decouples wall-normal momentum transfer mechanisms, suppressing turbulence within the lubricating layer and thus reducing overall drag. Conversely, for  $\lambda < 1.00$ , turbulence is sustained in the lubricating layer due to a higher local Reynolds number. In this regime, drag reduction is primarily due to the lower viscosity of the lubricating fluid, which directly decreases wall friction. Notably, an upper bound for  $\lambda$  exists beyond which drag reduction is not observed. At  $\lambda = 4.00$ , a slight drag enhancement was reported, suggesting that the turbulence suppression in the lubricating layer could not fully offset the increased friction from the more viscous fluid. The study meticulously dissects the energy balance within the lubricated channel. Using the energy-box representation, the authors provide a comprehensive visualization of energy fluxes. The balances of mean kinetic energy (MKE) and turbulent kinetic energy (TKE), derived from the Navier-Stokes equations, elucidate the intricate balance of production, transport, and dissipation of kinetic energy within the lubricated channel flow. In tensor notation, the MKE transport equation is expressed as:

$$\begin{aligned} \frac{D[MKE]}{Dt} = & - \left[ \langle u_i \rangle \left\langle \frac{\partial p}{\partial x_i} \right\rangle \right] \\ & + \left[ \langle u'_i u'_j \rangle \frac{\partial \langle u_i \rangle}{\partial x_j} \right] \\ & - \left[ \frac{\partial (\langle u'_i u'_j \rangle \langle u_i \rangle)}{\partial x_j} \right] \\ & + \left[ \frac{1}{2Re_\Pi} \frac{\partial^2 \langle u_i \rangle^2}{\partial x_j^2} \right] \\ & - \left[ \frac{1}{Re_\Pi} \frac{\partial \langle u_i \rangle}{\partial x_j} \frac{\partial \langle u_i \rangle}{\partial x_j} \right] \end{aligned}$$

Where:

- $\langle \cdot \rangle$  denotes ensemble averaging.
- $u_i$  is the  $i$ -th component of the mean velocity.
- $u'_i$  is the  $i$ -th component of the fluctuating velocity.
- $p$  is the pressure.
- $Re_\Pi$  is the power Reynolds number, defined as  $Re_\Pi = \frac{\rho u_\Pi h}{\eta_2}$ .

In which

1. Mean Pressure Gradient Term\*\*:  $-\left[\langle u_i \rangle \left\langle \frac{\partial p}{\partial x_i} \right\rangle\right] = \Pi_m$  Represents the power injected into the mean flow by the pressure gradient. This term is a source term for the MKE, as it injects energy into the system.
2. Production Term:  $\left[\langle u'_i u'_j \rangle \frac{\partial \langle u_i \rangle}{\partial x_j}\right] = P_k$  Represents the transfer of energy from the mean flow to the turbulent fluctuations. This term acts as a sink for MKE and a source for TKE.
3. Transport by Reynolds Stresses:  $-\left[\frac{\partial (\langle u'_i u'_j \rangle \langle u_i \rangle)}{\partial x_j}\right] = T_m$  Represents the redistribution of MKE due to Reynolds stresses. This term does not contribute to the net energy but redistributes it within the flow.

4. Viscous Diffusion of MKE:  $\left[ \frac{1}{2Re_{\Pi}} \frac{\partial^2 \langle u_i \rangle^2}{\partial x_j^2} \right] = D_m$  Represents the diffusion of MKE due to viscous effects. This term also acts as an internal transport mechanism.
5. Dissipation of MKE:  $-\left[ \frac{1}{Re_{\Pi}} \frac{\partial \langle u_i \rangle}{\partial x_j} \frac{\partial \langle u_i \rangle}{\partial x_j} \right] = \epsilon_m$  Represents the viscous dissipation of MKE. This term is a sink for MKE, converting kinetic energy into thermal energy.

By integrating the MKE and TKE equations over the wall-normal direction, we obtain the following balance equations:

$$\bar{P}_k + \bar{\Pi}_m + \bar{\epsilon}_m = 0,$$

where  $\bar{P}_k$ ,  $\bar{\Pi}_m$ , and  $\bar{\epsilon}_m$  are the integral forms of the production, mean pressure gradient, and dissipation terms, respectively.

$$-\bar{P}_k + \bar{\epsilon}_k = 0,$$

$\bar{\epsilon}_k$  is the integral form of the TKE dissipation term.

Combining the integral MKE and TKE balance equations, we get the total kinetic energy balance:

$$\bar{\Pi}_m + \bar{\epsilon}_m + \bar{\epsilon}_k = 0,$$

indicating that the total power injected into the system is ultimately dissipated by viscosity through both mean and turbulent viscous dissipation.

The findings underscore the significance of viscosity ratio and surface tension in modulating turbulence and achieving drag reduction.

## 2.2 Scale by scale energy budget

Wall-bounded turbulence integrates a complex interplay of processes that has impacts in both physical space and the space of scales. Marati, Casciola, and

Piva (2004) [28] explore this intricate phenomenon, focusing on the dual nature of energy fluxes in turbulent channel flows. Their investigation, grounded in the generalized Kolmogorov equation, clarifies how energy goes through various scales and spatial regions within a turbulent flow, particularly in the context of wall-bounded scenarios. As seen beforehand in these studies, the authors employ again Direct Numerical Simulation (DNS) to simulate a turbulent channel flow at a friction Reynolds number  $Re_\tau = 180$ . The computational domain is configured as  $(4\pi h, 2h, 2\pi h)$ , where  $h$  again denotes the channel half-height. This setup ensures statistical homogeneity in the streamwise ( $x$ ) and spanwise ( $z$ ) directions, while maintaining no-slip conditions at the walls. The flow is driven by a mean pressure gradient, ensuring a constant mass flux through the channel. The core of the study revolves around the generalized Kolmogorov equation, which extends the classical framework to account for inhomogeneities and anisotropies inherent in wall turbulence. This generalized form is articulated as:

$$\begin{aligned} & \frac{\partial \langle \delta u^2 \delta u_i \rangle}{\partial r_i} + \frac{\partial \langle \delta u^2 \delta U_i \rangle}{\partial r_i} + 2 \langle \delta u_i \delta u_j \rangle \frac{\partial \delta U_i}{\partial r_j} + \frac{\partial \langle u_j^* \delta u^2 \rangle}{\partial X_{cj}} + \frac{\partial \langle \delta u^2 U_j^* \rangle}{\partial X_{cj}} \\ & + 2 \langle u_j^* \delta u_i \rangle \frac{\partial \delta U_i}{\partial X_{cj}} = -4 \langle \epsilon^* \rangle + 2\nu \frac{\partial^2 \langle \delta u^2 \rangle}{\partial r_i \partial r_i} - \frac{2}{\rho} \frac{\partial \langle \delta p \delta u_i \rangle}{\partial X_{ci}} + \nu \frac{\partial^2 \langle \delta u^2 \rangle}{\partial X_{cj}^2}, \end{aligned}$$

where  $\delta u_i = u_i(\mathbf{x} + \mathbf{r}) - u_i(\mathbf{x})$  denotes the velocity increment, and the asterisk denotes a midpoint average. This equation encapsulates the spatial redistribution and scale-to-scale energy transfer within the turbulent flow. The investigation reveals that the energy fluxes in wall turbulence exhibit distinct behaviors across different regions of the flow:

1. **Viscous Sublayer:** Dominated by viscous effects, the scale-to-scale transfer of energy is negligible. Instead, local production and dissipation of turbulent kinetic energy (TKE) dominate the dynamics.

2. **Buffer Layer:** Identified as the engine of turbulence, this region sees a significant imbalance where the production of TKE exceeds dissipation. The surplus energy cascades through scales, feeding the turbulence in adjacent regions. The spatial flux of TKE generated in the buffer layer is crucial in sustaining turbulence throughout the channel.
3. **Logarithmic Layer:** Here, production and dissipation reach an equilibrium. The turbulent transport of scale energy, driven primarily by the mean shear, becomes significant. This layer exhibits classical inertial scaling behaviors, and the fluxes of scale energy align with the predictions of the generalized Kolmogorov framework.
4. **Core Region:** Turbulence in this region is maintained by the spatial flux of TKE from the buffer layer. The production-to-dissipation ratio approaches unity, and the energy dynamics are governed by the spatial redistribution of energy generated nearer to the walls.

The study meticulously details the balance of scale energy fluxes. The generalized Kolmogorov equation is employed to derive insights into the mechanisms of energy production, cascade, and dissipation:

$$\nabla_r \cdot \Phi_r + \frac{\partial \Phi_c}{\partial Y_c} = s(r, Y_c),$$

$$s(r, Y_c) = -2 \langle \delta u \delta v \rangle \left( \frac{dU}{dy} \right)^* - 4 \langle \epsilon^* \rangle,$$

where  $\Phi_r$  denotes the scale-energy flux in the space of scales, and  $\Phi_c$  represents the flux in physical space. The source term  $s(r, Y_c)$  encapsulates the contributions of the production and dissipation of the scale energy. The analysis demonstrates that in the log-layer, the balance is predominantly influenced by production and cascade mechanisms. The effective production  $\Pi_e(r, Y_c)$  and effective dissipation  $E_e(r, Y_c)$  are crucial in describing the energy dynamics:

$$\Pi_e(r, Y_c) = \Pi(r, Y_c) + T_c(r, Y_c) - P(r, Y_c),$$

$$E_e(r, Y_c) = E(r, Y_c) + D_r(r, Y_c) + D_c(r, Y_c).$$

In the buffer layer, the analysis reveals a marked production of scale energy, which is redistributed by the turbulent transport component of the spatial flux. This redistribution is vital in sustaining turbulence across the channel. The authors provide a comprehensive exploration of energy cascade and spatial fluxes in wall turbulence, leveraging the generalized Kolmogorov equation to unravel the complex interplay of scale energy transfers and spatial redistributions. Their findings emphasize the critical role of the buffer layer as the powerhouse of turbulence, feeding energy into the system and sustaining turbulent fluctuations across various scales and regions within the channel. This study not only reinforces classical turbulence theories but also offers new insights into the behaviors of wall-bounded turbulent flows.



# Chapter 3

## Methodology

We consider a configuration with two immiscible fluids in a plane channel. The non-dimensional Navier-Stokes equations for two phase incompressible Newtonian fluids can be written as

$$\nabla \cdot \mathbf{u} = 0, \quad (3.1)$$

$$\frac{\partial \mathbf{u}}{\partial t} + \mathbf{u} \cdot \nabla \mathbf{u} = -\nabla p + \frac{1}{Re} \nabla \cdot \mathbf{T} + \frac{1}{We} \mathbf{f}_\sigma \quad (3.2)$$

where  $\mathbf{u} = \bar{\mathbf{u}}(\mathbf{x}) + \mathbf{u}'(\mathbf{x}, t)$  is the velocity field, divided into a mean component and a fluctuation term (marked with the apex '). Since we are considering a fully developed turbulent flow, for our purposes the mean velocity field here is the average over time, streamwise and spanwise directions. We will assume the following notation for the components of the velocity field

$$\mathbf{u}(\mathbf{x}, t) = \begin{pmatrix} u(\mathbf{x}, t) \\ v(\mathbf{x}, t) \\ w(\mathbf{x}, t) \end{pmatrix}. \quad (3.3)$$

The other quantities in eq.3.2 are  $p = p(\mathbf{x}, t)$  which represents the pressure,  $\rho = \rho(\mathbf{x}, t)$  the density,  $\mu = \mu(\mathbf{x}, t)$  the dynamic viscosity,  $\mathbf{f}_\sigma = \mathbf{f}_\sigma(\mathbf{x}, t)$  the force per unit volume due to surface tension.  $\mathbf{T} = 2\mu\mathbf{S}$  is the viscous stress tensor,

where  $\mathbf{S} = [\nabla\mathbf{u} + \nabla\mathbf{u}^T]/2$  is the strain-rate tensor.  $Re$  and  $We$  are respectively the Reynolds number and the Weber number, defined as

$$Re = \frac{\tilde{U}\tilde{L}\tilde{\rho}}{\tilde{\mu}}, \quad We = \frac{\tilde{\rho}\tilde{U}^2h}{\tilde{\sigma}}, \quad (3.4)$$

Where  $\tilde{U}$ ,  $\tilde{L}$ ,  $\tilde{\rho}$ ,  $\tilde{\mu}$ ,  $\tilde{\sigma}$ , are the reference quantities used to obtain the non-dimensional governing equations. In order we have velocity, length, density, dynamic viscosity, surface tension.

### 3.1 Volume Of Fluid

As introduced in Chapter 1, the Volume of Fluid (VOF) method is a widely used interface-capturing technique for two-phase flows. Here, we provide a detailed description of its implementation in our simulations, focusing on the specific numerical techniques and setup that enabled our investigation.

Multiphase flows, particularly those undergoing phase change, present themselves in both an environmental and economic context. Cloud formation and rain, filled cooling towers, wet scrubbers and spray combustion all involve the interaction of numerous phases, exchanging mass/momentum/energy dynamically through interfaces as they develop. The interfaces in such systems are typically orders of magnitude thinner than other scales in the problem. One must use a sophisticated modeling approach, which treats them as infinitesimally thin layers and which reduces interphase coupling conditions down to transport balances and thermodynamic relationships. Despite such simplifications, direct numerical simulations (DNS) that explicitly resolve interfaces are still a computational burden. Interface-resolved simulations fall into two general methods: interface-tracking and interface-capturing. In interface-tracking methods such as front-tracking, the interface is explicitly defined by Lagrange markers, which move with the flow but while visualising interfaces accurately, these methods struggle with complex topological changes. Interface-capturing methods, on the

other hand, use methods such as level-set, volume-of-fluid (VoF) and diffuse interface methods, in these methods the interface is represented implicitly by solving transport equations for scalar field (s) that define where the interface happens. These methods have a more natural handling of topological changes, but can be less accurate in terms of calculating such interface properties as curvature or normals. In this context Scapin et al. [21] present a volume-of-fluid method for interface-resolved simulations of two-fluid flows. The method proposed is included in a highly efficient FFT-based two-fluid Navier-Stokes solver and uses algebraic VoF techniques for interface representation. The solver and method are extended to allow consideration of thermal energy and vaporized liquid mass transport. A novel approach to interface velocity computation provides accurate mass conservation, applicable to both algebraic and geometrical VoF methods. The method is rigorously verified and validated against several benchmarks, with good mass conservation and overall performance, which demonstrates its excellence.

The force per unit volume due to surface tension is defined as

$$\mathbf{f}_\sigma = \sigma k \mathbf{n} \delta, \quad (3.5)$$

where  $k$  the curvature of the interface,  $\mathbf{n}$  the normal vector,  $\delta$  the Dirac function. This latter can be approximated by  $\nabla \phi$ , in which  $\phi$  is the *Volume of Fluid* (VOF) fraction across the interface. In particular  $\phi = 0$  in fluid 1, while  $\phi = 1$  in fluid 2 and  $0 < \phi < 1$  at the interface.

Following the general VOF framework outlined in Chapter 1, we employ the *MTHINC* (multidimensional tangent of hyperbola for interface capturing) method for the interface reconstruction [30, 23], which approximates the color function  $H(\mathbf{x})$  using a multidimensional hyperbolic tangent profile given by the function

$$H(\mathbf{x}) \approx \widetilde{H}(\mathbf{x}) = \frac{1}{2}(1 + \tanh(\beta(P(\mathbf{x}) + d)), \quad (3.6)$$

in which  $\mathbf{x} \in [0, 1]$  is a local coordinate system in each cell,  $\beta$  is a constant parameter that represents the slope of the approximate Heaviside function,  $d$  a normalization parameter and  $P(\mathbf{x})$  a linear or quadratic surface function. The linear expression is given as

$$P(x_j) = a_j x_j, \quad (3.7)$$

where the coefficients  $a_j$  can be algebraically determined by imposing the components of the normal values and the curvature tensor for  $P$ . The parameter  $d$  can be obtained through the constraint

$$\int_{\mathbf{x} \in (0,1)} \widetilde{H(\mathbf{x})} d\mathbf{x} = \phi. \quad (3.8)$$

Once the normal vector defined as  $\mathbf{n} = \nabla\phi / \|\nabla\phi\|$  is known, the curvature  $k$  is given by  $\partial n_i / \partial x_i$ . Approximating the interface location  $\delta \approx \|\nabla\phi\|$ , the surface tension force can be written as

$$f_{j\sigma} = \sigma k n_j \delta \approx \sigma k \frac{\partial \phi}{\partial x_j}. \quad (3.9)$$

It has been proved that in most cases VOF results are more accurate compared to the Phase field at the same resolution [31]. The computational cost of the Diffusive Interface is instead typically of an order of magnitude less than VOF at the same resolution.

## 3.2 Incompressible Two-Fluid Flow Solver

For accurate simulations in the context of incompressible two fluid flow, a precision at the highest possible level in both space and time is necessary. Unique challenges need to be addressed when dealing with strong discontinuities of the interface, such as in scenarios where the density ratio differs between the fluids for several order of magnitude (as in the air-water system, where the ratio is 1000). These kinds of discontinuity invalidate simplified methods, like

the Boussinesq approximation and need to be directly addressed.

The main issue when approaching this kind of problem is mainly computational cost and efficiency. The Volume of Fluid (VOF) method, discussed in the section above, is often associated with the projection method when solving an incompressible fluid dynamic problems. This latter works by decoupling the velocity field from the pressure field, which is crucial when dealing with interface instabilities because it provides the flexibility to handle large variations in pressure and velocity across the interface without including the instability into the solution. Following then an iterative process ensures the convergence to a stable solution, reducing the error while maintaining the incompressibility constraint. One goal required in practical applications is often the second order accuracy and stability.

Many numerical methods have been developed for this purpose, among those one of the most prevalent techniques is the pressure-correction method, which requires the numerical solution of a Poisson equation for pressure at each time step. In particular, this method developed in 1986 by Jos J. van Kan [37] results second-order accurate in time and space. The advanced van Kan method solves the Navier-Stokes equations for incompressible viscous flow using a Crank-Nicolson type scheme for the prediction step. The projection method is a particular type of pressure-correction method where the incompressibility condition required is achieved by first predicting the velocity field without considering the pressure and then correcting this term through the solution of the Poisson equation for the pressure. This technique has been widely adopted and represents a standard due to its reliability and robustness displayed in a vast range of fluid dynamics applications. The key aspects of this scheme are presented here. Solving a fluid dynamic incompressible problem with this approach typically involves the following steps:

- Discretization. To reduce the computational domain to a discrete space (grid points). The Navier-Stokes and Continuity equations are then solved in the discretized domain.
- Prediction Step. Solving the momentum equation for the velocity field ( $\mathbf{u}^*$ ) without taking into account the pressure gradient.

$$\frac{u^* - u^n}{\Delta t} = -(u^n \cdot \nabla)u^n + \nu \nabla^2 u^n + f^n,$$

where  $\mathbf{u}^n$  is the velocity at the previous time step,  $\nu$  is the kinematic viscosity, and  $\mathbf{f}^n$  represents external forces.

- Pressure Poisson Equation. The Pressure Poisson equation is formulated to guarantee a divergence-free velocity field.

$$\nabla^2 p^{n+1} = \frac{1}{\Delta t} \nabla \cdot u^*.$$

- Solving the Poisson Equation. The main advantage of Van Kan's strategy is the reduction of the Poisson equation to a one-dimensional problem that can be solved sequentially. This technique increases not only the stability but also the efficiency, due to the lower complexity. The Fast Fourier Transform (FFT) transforms the spatial domain into a frequency domain allowing a significant increase of the speed process. This approach is highly beneficial, in particular, with large-scale problems reducing the computational effort required for solving the equation.
- Correction Step: Correct the velocity term with the computed pressure.

$$u^{n+1} = u^* - \Delta t \nabla p^{n+1}.$$

This ensures the velocity field is divergence-free:

$$\nabla \cdot u^{n+1} = 0.$$

This approach has been largely validated in both laminar and turbulent scenarios and has proven its potential in handling a high Reynolds number and complex geometry. In the context of the Van Kan pressure correction scheme, another key component is the calculation of quantities on staggered grids, in contrast to the collocated grid, where all variables are calculated at the same location. There is no necessity, from a theoretical point of view, to allocate all variables in the same place. In contrast, the staggered arrangement introduced in 1965 by Harlow and Welsh [38] leads to a number of advantages. The main advantage with this layout is the strong decouple connection between the velocities and the pressure to avoid the convergence problem and spurious pressure oscillations. In this work we did not need to study the mesh convergence as we relied on the same grid validated in the paper related to the code developed by KTH Royal Institute of Technology in Stockholm used to perform all the simulations [21]. In their paper, the authors employ a uniform Cartesian mesh with a staggered layout. The second order accuracy in space was demonstrated by the central difference discretization while the second order accuracy in time via Crank–Nicolson for diffusion and Adams–Bashforth for advection. Because the convergence of the uniform staggered grid had already been established, we had the possibility to focus on the physics that underpin the phenomenon of the Drag Reduction with the novel approach of the VOF method.

### 3.3 Simulations set-up

For all simulations, the flow is periodic in the streamwise  $x$  and spanwise  $y$  directions, with no-slip conditions in the normal direction  $z$  and is driven by a constant pressure gradient. The channel dimensions are  $L_x \times L_y \times L_z = 8h \times 4h \times 2h$ , with  $h$  the half-channel height, the grid we used is  $N_x \times N_y \times N_z = 384 \times 192 \times 284$ . The reference position of the interface is located at  $1.85h$ , which separates a lubricating layer of fluid with kinematic viscosity  $\nu_1$  from a thicker main layer

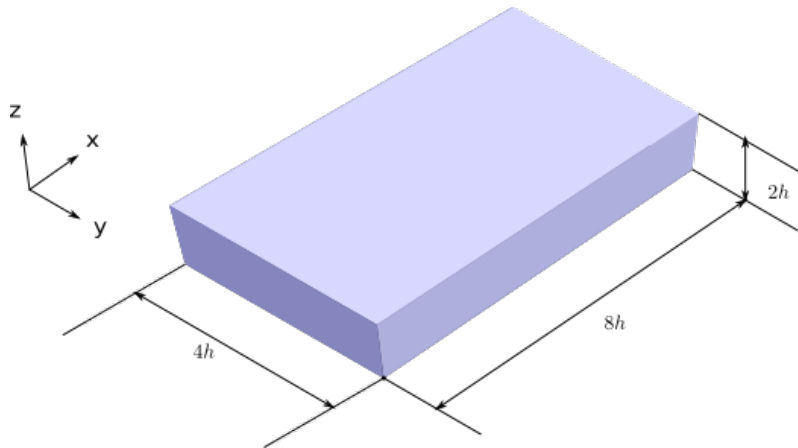


Fig. 3.1 Sketch of the computational domain of the channel.

of fluid with kinematic viscosity  $\nu_2$ . The two fluids have the same density.

One of the goals of the present work is to investigate the role of the interface along with the viscosity ratio in the mechanism that produces the drag reduction. Starting with a single phase flow, all simulations are performed with an initial Poiseuille profile perturbed by a finite amplitude disturbance. The film is added once the statistically steady state condition is reached. In two fluid flows, the value of the surface tension characterizes the behavior of the interface. In our simulations the variations in surface tension appear in terms of a Weber number (eq.3.4), which represents a ratio between deforming inertial forces and cohesive forces, namely the surface tension force. In this way for high values of  $We$  we get more easily deformable interfaces, while for low  $We$  more stable interfaces. All our simulations are run at a shear Reynolds number  $Re_\tau = u_\tau h / \nu_2 = 100$ , where, as customary (see the definition from eq.1.15),  $u_\tau = \sqrt{\bar{\tau}} / \rho$  (with  $\sqrt{\bar{\tau}}$  being the wall shear stress) is the friction velocity and  $\nu = \mu_2 / \rho_2$  is the kinematic viscosity of the fluid in the thicker layer.

Unless otherwise stated, we have used as friction units those obtained considering the value of the wall shear stress calculated as the average between the two walls. This procedure has the effect that the normalization is the same for all the simulations regardless of the fact that locally at each of the

---

two walls the viscous units would be different. In order to better investigate the dynamic of the interface for the case  $\lambda = 1$  we investigate two cases with different Weber number,  $We = 0.055$  and  $We = 0.5$ . The amount of data considered for the statistics is selected to ensure the statistical convergence. For the simulation has been run the open source code developed by *KTH* Royal Institute of Technology in Stockholm [21]. During our analysis, we refer for comparison to the aforementioned work by Ahmadi et al. [19, 28], which reports results of a turbulent channel flow with a lubricating film on one wall. It is worth pointing out that the parameters explored in their study are slightly different and we will address the implications further on.



# Chapter 4

## Results

This chapter highlights the main findings of this thesis. In particular, it builds up and extends the results already published in our paper and adds the preliminary developments on the two-points scale energy budget. The latter provides a meaningful insight on the dynamic of turbulence through the extension of the Kolmogorov equation to inhomogeneous and anisotropic conditions. We begin by presenting the classic statistics of single turbulent channel flow, extended to our two-phase problem reporting as a reference the single-phase case. These statistics include the discussion on the mean streamwise velocity, which represents the most straightforward visualisation prove of the drag reduction as well as the volume flow rate, which is shown to increase in all studied cases with respect to the single phase. We then examine other statistics already introduced in the first chapter, such as the analysis of the root-mean square (RMS) velocity fluctuations, which provides insight into the turbulence intensity distribution along the wall normal direction and the profiles of the viscous shear stress. Root-mean square vorticity fluctuations are also taken into account to investigate the dynamic behavior of the vortices and their impact on the flow, particularly in the region near the interface. To gain a further understanding of the effects of turbulence around this region, the probability density functions (PDF) of the normalized Wall-Shear stress fluctuations and the interface elevation are also included along with their Joint

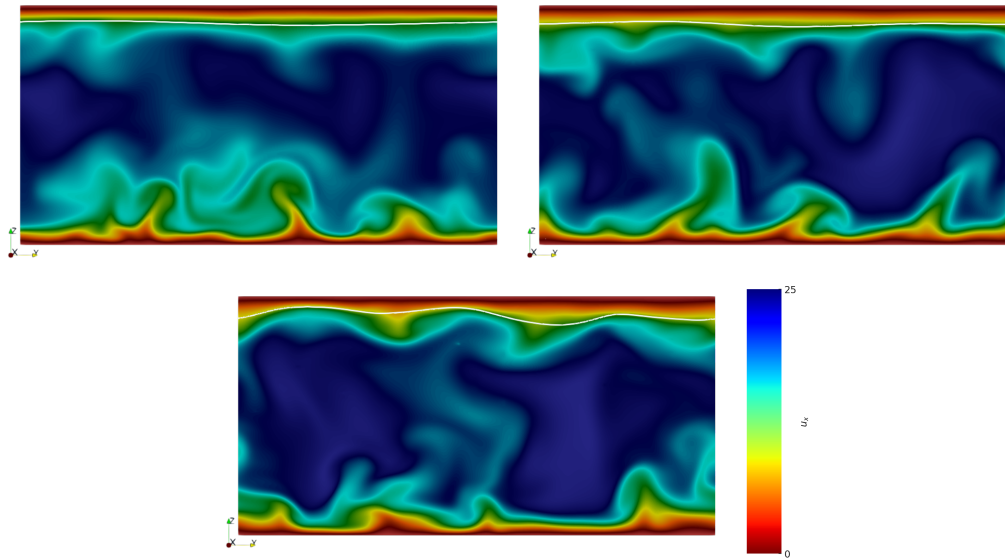


Fig. 4.1 Cross-section ( $y - z$ ) of the instantaneous streamwise velocity  $u$ . In the top left panel the case with  $\lambda = 0.5$ . Top right panel refers to the case with  $\lambda = 1$ . Bottom panel the case  $\lambda = 1$ ,  $We = 0.5$ . The white line marks the position of the interface.

Probability Density Function (JPDF). The final part of the statistical analysis explores the contribution to the drag reduction of the energy budgets.

## 4.1 Results and Discussion

In Fig.4.1 we report the contours of the streamwise velocity  $u$  in a cross-section of the channel for the three cases with the lubricating layer together with the position of the interface identified with a white line. The top left panel shows the case with  $\lambda = 0.5$  while the right and bottom panels refer to the case with  $\lambda = 1$ . Already at first glance, the analysis of the top left panel seems to suggest that in the lubricating layer we have a laminar behaviour with no evidence of turbulence. This can be related to the DR mechanism that damping the turbulent fluctuations produces a relaminarization of the layer. When the viscosity for the two fluids is the same in the case with  $We = 0.055$  (Fig.4.1, top right panel) we can still appreciate how the presence of an interface affects the dynamics near the lubricated wall. Considering the case with  $We = 0.5$

we can notice a slight increase of turbulence compared to the previous case probably induced by a larger deformation of the interface. We continue the analysis reporting the wall normal behavior of the mean streamwise velocity profile (Fig.4.2). The first thing that we notice for all studied cases is that the presence of the lubricating layer produces an asymmetric velocity profile. When considering simulations with constant pressure gradient, this is balanced by the viscous shear stress at the walls. By observing that the gradient in the non-lubricated wall increases for both  $\lambda$  values we expect that the value of the shear stress should in both cases decreased at the other wall (see also Fig.4.4). What we see is that for the case with the lower viscosity at the lubricated wall ( $\lambda = 0.5$ ) this is compatible with an increase of the velocity in the region close to the lubricated layer, while for the case when the viscosities are the same ( $\lambda = 1$ ) this has to come with a smaller velocity gradient at the wall. The case with  $We = 0.5$  is not reported here because basically identical to the other case with  $\lambda = 1$ .

In Table 4.1 we show the behavior of the total volume flow rate  $Q$  of the two layers and the wall shear stress  $\tau_w$  at both walls taking the Single Phase value as a reference. As a consequence of the presence of the interface there is a gain of the volume flow rate. This increase reaches its maximum ( $\simeq 22\%$ ) for  $\lambda = 0.5$ . When the viscosity of the two fluids is the same, the increase of the volume flow rate ( $\simeq 7\%$ ) for lower Weber, while for  $We = 0.5$  is slightly

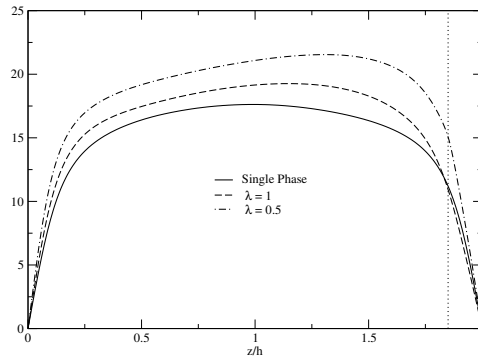


Fig. 4.2 Normalized mean streamwise velocity  $\bar{u}^+$  as a function of the wall-normal direction for all the simulated cases. The dotted line at  $z = 1.85$  marks the mean interface position.

Table 4.1 Volume flow rate  $Q/Q_{SP}$  normalized by the reference Single Phase along with the wall shear stress for the different cases (*SinglePhase(SP)*,  $\lambda = 1$ ,  $\lambda = 0.5$ ) at the bottom wall ( $\bar{\tau}_{w,b}$ ) and top wall ( $\bar{\tau}_{w,t}$ ).

Case	$Q/Q_{SP}$	$\bar{\tau}_{w,b}/\bar{\tau}_{SP}$	$\bar{\tau}_{w,t}/\bar{\tau}_{SP}$
SP	1	1	1
$\lambda = 1, We = 0.055$	1.074	1.165	0.824
$\lambda = 1, We = 0.5$	1.083	1.194	0.816
$\lambda = 0.5, We = 0.055$	1.223	1.392	0.580

higher ( $\simeq 8\%$ ). This suggests that the drag reduction is already in place, so that the mechanism stems from the presence of the interface. Compared to the work of Ahmadi et al. ([19]), we do not observe here any inflection point close to the interface.

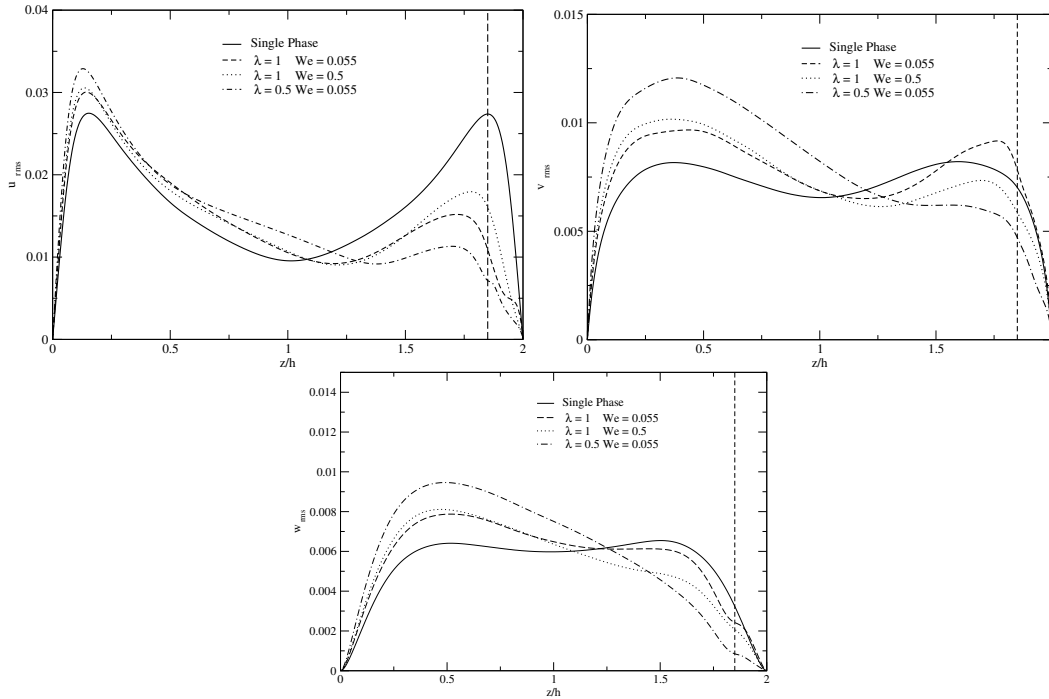


Fig. 4.3 Root-mean square velocity fluctuations for single phase and viscosity stratified flows along the  $z$  axis. Streamwise component  $u_{rms}$  left panel above, spanwise component  $v_{rms}$  right panel above, wall-normal component  $w_{rms}$  bottom panel. The dotted line at  $z = 1.85$  marks the mean interface position.

To better understand the connection between the dynamic of turbulence and the viscosity, we analyse the root mean square (RMS) velocities in the homogeneous and wall normal directions. The velocity fluctuation intensities can provide an idea of the structure of turbulence. We start by examining the streamwise velocity fluctuations,  $u_{rms}$ , in the top left panel in Fig.4.3. The profile of the SP presents its maximum close to the walls and is symmetrical to the center line, as expected when the statistics has reached the steady state. Fluctuations are higher at the vicinity of the walls, where the velocity gradients are larger. The behavior at the non lubricated wall does not change remarkably varying the parameters, in particular we can see that values in that region increase as  $\lambda$  decreases as we expected from the observation of the mean velocity. On the other hand the behavior at the lubricated wall is very different. Regardless the viscosity, we observe a strong reduction of turbulence. We can therefore confirm that relaminarization is taking place in this region. This process intensifies as  $\lambda$  decreases. It is worth noting that the  $u_{rms}$  profile does not show the presence of the interface when the two fluids have the same viscosity, on the hand we observe an inflection point when viscosity changes across the interface. We present the values of the spanwise component  $v_{rms}$  in the right panel of Fig.4.3. As for the streamwise one, the fluctuations are minimal when the value of the viscosity in the lubricating layer is halved. Regarding the cases at  $\lambda = 1$ , we see that the fluctuating component overcomes that of the single phase at the lubricated wall for the smaller Weber number. The behaviour of the wall-normal component  $w_{rms}$  (bottom panel of Fig.4.3) is again qualitatively close to that of the spanwise one, with larger fluctuations for the case with  $\lambda = 1$ ,  $We = 0.055$ . It worth observing that in this component we do have an inflection point when the Weber number is small suggesting that a larger surface tension might be responsible for this behaviour. These results differ widely from the ones obtained by Ahmadi et al.[19], where a local minimum close to the reference location of the interface is observed in most of

the components.

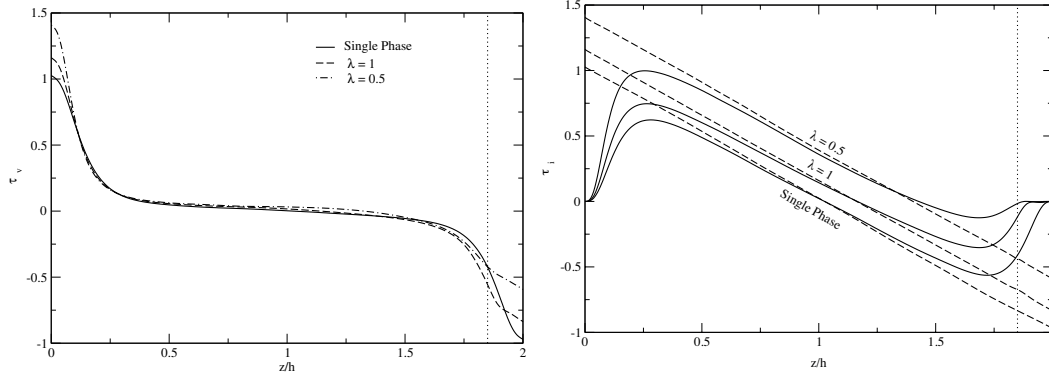


Fig. 4.4 Profile of the viscous shear stress  $\bar{\tau}_v^+$  in the left panel. Turbulent shear stress  $\bar{\tau}_t^+$  and the two contributions together  $\bar{\tau}_v^+ + \bar{\tau}_t^+$ , respectively continuous and dashed line on the right panel. The dotted line at  $z/h = 1.85$  marks the mean interface position.

To gain further understanding on the observed DR, we start looking at the contributions to the shear stress. In Fig.4.4 top panel we can see the trend of the viscous shear stress. At the not-lubricated wall layer, profiles have qualitatively the same trend of the SP case, with larger values of the shear as expected from the behaviour of the mean velocity, Fig. 4.2. As  $\lambda$  decreases, the decrease of the shear stress at the lubricated wall produces an equal increase at the non lubricated wall due to the fact that the total shear stress must balance with the applied pressure gradient, which in all our simulations has a constant value. It is interesting to note that for  $\lambda = 0.5$  in the low viscosity layer we can observe a basically linear profile, typical of laminar fluids. This is an evidence that of a relaminarization effect. We can now extend the analysis to the other stress contributions. In general, the total stress in two-phase flows is given by the sum of three contributions, the viscous shear stress, the turbulent stress and a further contribution produced by the surface tension. We display in the bottom panel of the Fig.4.4 the turbulent stress profile along with the sum of this with the viscous term for the different cases examined,

$$\bar{\tau}_v^+(z) + \bar{\tau}_t^+(z) = \nu^+(z) \frac{\partial \bar{u}^+}{\partial z^+} - (\overline{u'w'})^+. \quad (4.1)$$

In a fully developed turbulent channel flow, the integral of the momentum equation with respect to the wall normal direction, produces a linear relation between the constant pressure gradient and the total shear stress. It is therefore possible to estimate the contribution of the capillary stress as a difference from the other two. The deviation from this straight line then gives us a measure of the magnitude of this quantity. We can accordingly infer from Fig.4.4 that this contribution in our numerical results is basically negligible. The variation of the Weber number does not produce here any significant change of the trend at  $\lambda = 1$ , so for simplicity we decided not to report the relative profile. It is important to mention that this behaviour is again different from the one reported in Ahmadi et al. ([19]), leading us to conclude that in our case even if we observe a similar effect in terms of Drag Reduction we cannot directly link the observed changes to the presence of strong capillary stress contribution in the mean momentum.

We continue our analysis taking into account the vorticity field which is defined as  $\boldsymbol{\omega} = \nabla \times \mathbf{u}$ . In particular we will analyse the wall normal behaviors of the fluctuating components along homogeneous and wall-normal directions defined as

$$\boldsymbol{\omega}'_{rms} = \begin{pmatrix} \frac{\partial w'}{\partial y} - \frac{\partial v'}{\partial z} \\ \frac{\partial u'}{\partial z} - \frac{\partial w'}{\partial x} \\ \frac{\partial v'}{\partial x} - \frac{\partial u'}{\partial y} \end{pmatrix}. \quad (4.2)$$

In Fig.4.5 we report the rms vorticity profiles. For the single phase all profiles are again symmetric to the centreline of the channel as they are supposed to be when the flow has reached the statistically steady state. We see again that the symmetry is lost by introducing the lubricated layer due to the change of the dynamic behaviour of the flow. As for the turbulent fluctuations, at the not-lubricated wall, we see that the amplitudes of the vorticity fluctuations exhibit larger values, compatibly with larger shear at the wall. At the lubricated

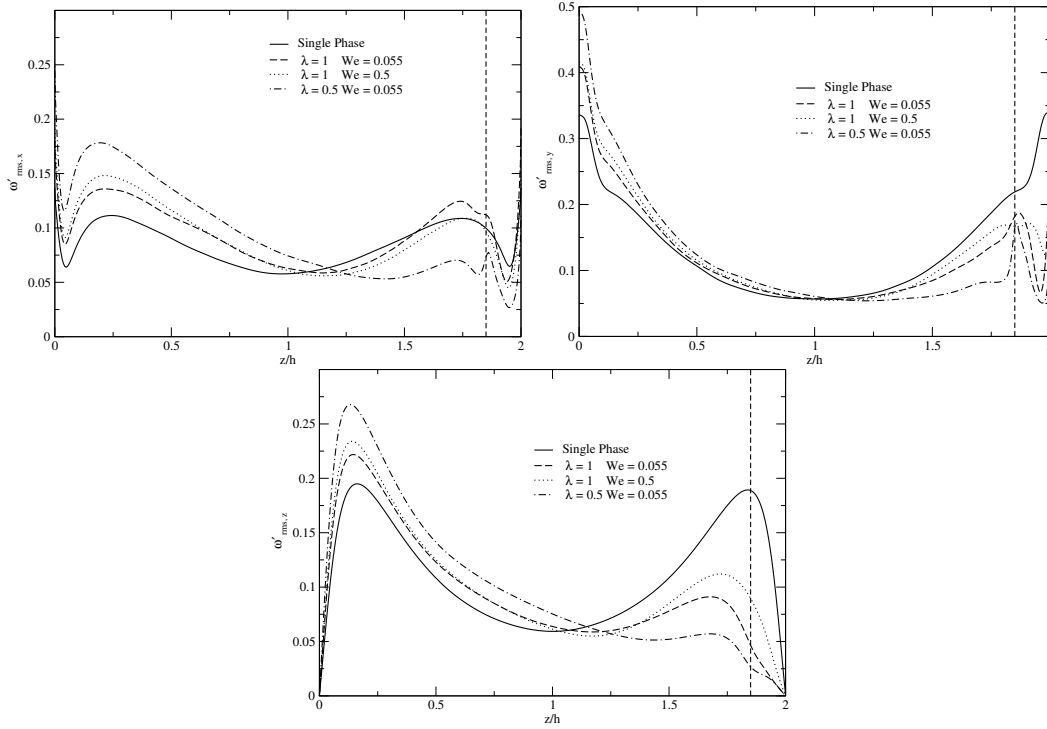


Fig. 4.5 Root-mean square vorticity fluctuations for all the simulated cases along the normal axis. Streamwise component  $\omega'_x$  left panel above, spanwise component  $\omega'_y$  right panel, wall-normal component  $\omega'_z$  below. The dotted line at  $z = 1.85$  marks the mean interface position.

wall, the homogeneous components of the vorticity,  $\omega'_{x,rms}$  and  $\omega'_{y,rms}$ , can be described in a similar terms. An effect of the interface is clearly observable. In particular, for the two cases with the larger value of the Weber number, we can observe that at the interface the behavior of the fluctuations recalls somehow the one at the wall in the non lubricated case. This occurrence is particularly true for the case at  $\lambda = 0.5$ , reported with the dash-dotted curves in Fig.4.5. Indeed the top left panel, showing the streamwise component we observe a local maximum at  $z/h = 1.7$  followed by a local minimum. On the other hand, in the right panel the  $\omega'_{y,rms}$  just before the interface shows an inflection point followed by an increase at interface location. A much smoother behaviour of the curves is indeed observed for the larger Weber number. Finally, in the lubricating layer for  $z/h > 1.85$ , the dynamics of the fluctuations in the homogeneous directions show basically the same behavior. Starting from the value of the fluctuations at the interface location, we can appreciate a sharp

drop followed by a recovery at the wall. Those extrema represent vortices with opposite sign and their location corresponds to the location of the centre of the vortices [34].

Generally speaking, the presence of the interface (the dotted line in the figure) seems to decouple the dynamics of the vorticity between the two layers. This observation seems to apply specially to the cases with the smaller value of the Weber number, where the larger value of the surface tension inhibits large excursions of the interface. The wall-normal component of the vorticity,  $\omega'_{z,rms}$ , instead is not influenced by the presence of the interface as much as the other components arguably because associated to wall-parallel motions which are less affected by the surface tension forces for limited interface deformations. Only the case with  $\lambda = 0.5$  shows at the top wall an inflection point near the interface.

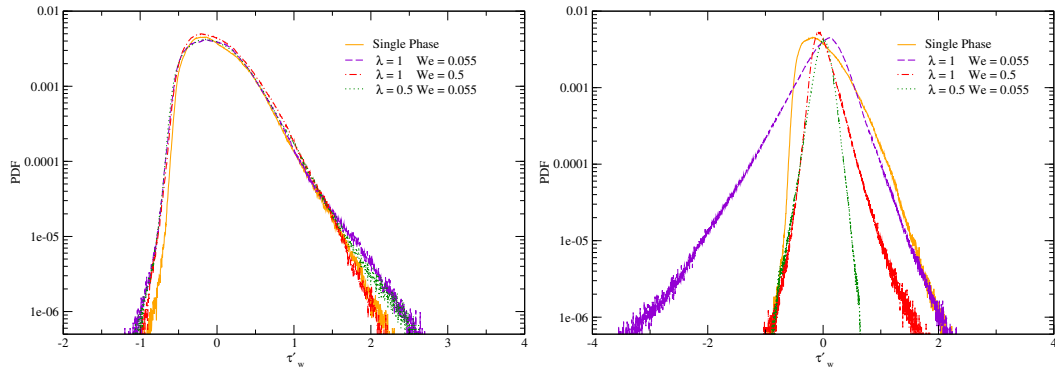


Fig. 4.6 Probability Density Function (PDF) of the normalized Wall-Shear stress fluctuations  $\tau'_w = (\tau_w - \bar{\tau}_w)/\bar{\tau}_w$  for all cases. Profiles at the non lubricated wall are on left panel, while the the right panel refers to the lubricated wall.

## 4.2 Probability density functions

To understand the dynamics of the flow in the presence of the interface we computed the Probability Density Function (PDF) of the shear stress at both walls. In fig.4.6 we show in semi-logarithmic scale the PDF of the wall shear stress fluctuations  $\tau'_w$  defined as

$$\tau_w' = \frac{\tau_w - \bar{\tau}_w}{\bar{\tau}_w} \quad (4.3)$$

where  $\bar{\tau}_w$  is the mean value calculated at the wall we are considering.

At the non lubricated wall all profiles are asymmetrical with a larger ratio of positive values that implies a higher probability occurrence of positive fluctuations. In general, we notice that the shape of the PDF for the two-phase flow do not significantly differ from the single-phase case, this means that the presence of the interface does not affect the dynamic near the opposite wall. We only appreciate a slightly different behavior of the tails of the PDFs. The increase probability of larger fluctuations can be traced back to the mean shear stress at the wall as discussed in the previous paragraph. At the lubricated wall the PDFs are instead drastically different from those of the single-phase case. While the latter is statistically identical to the non lubricated wall, the shape shows substantial differences as  $\lambda$  and  $We$  change [19]. In the case when the two fluids have the same viscosity and  $We = 0.055$  the profile is shifted towards negative values. In particular when  $\tau_w' < -1$ , the change of sign with respect to the average, suggests the presence of reverse recirculation areas in which  $\tau_w$  locally changes sign. It is interesting to notice that this large negative fluctuations disappear in the case in which the  $We$  number is higher, namely  $We = 0.5$ . Notwithstanding this observation the presence of positive fluctuations seem to suggests that the turbulence activity is still in place compared to the case with lower viscosity ratio. In fact, as  $\lambda$  decreases we see that the curve is confined around the value  $\tau_w = 0$ . The reduction of the shear stress fluctuations confirms the presence of a relaminarization mechanism.

We compare in Fig.4.7 the PDF of the interface elevation  $\eta$  for the different cases, taking into account the effects of the viscosity ratio and the Weber number. For all the cases the PDF of the interface is nearly symmetric around the value  $z/h = 1.85$ , namely the reference position of the interface. The effect

of the Weber number is consistent with the expectations. When  $We = 0.055$  the the PDF is slightly taller and narrower close to the most probable value. A lower surface tension instead, allows a more deformable interface, so the PDF widens for the case  $We=0.5$ , see also the instantaneous position in Fig. 4.1. Decreasing the viscosity ratio to  $\lambda = 0.5$  with  $We = 0.055$  instead the shape of the pdf is sharper and constrained around the average position of the interface where it takes its maximum vale. This behavior occurs as a consequence of the turbulence reduction when decreases the viscosity ratio.

To better investigate the correlation between the interface deformation and the shear stress we show in fig. 4.8 the Joint Probability Density Functions (JPDF) between the normalized interface elevation  $\eta^+ = u_\tau(\eta - \bar{\eta})/\nu$  and the normalized wall-shear stress fluctuations  $\tau'_w = (\tau_w - \bar{\tau})/\bar{\tau}$  for  $\lambda = 1$  and the two values of the Weber number under consideration. The contour plot of the two-dimensional JPDF are shown only for the lubricated wall. We observe that the different value of the Weber number has a strong effect on the structure of the correlation. For the case with  $We=0.055$  there is an anti-correlation between the shear and the interface deformation mostly when the  $\eta^+$  takes positive

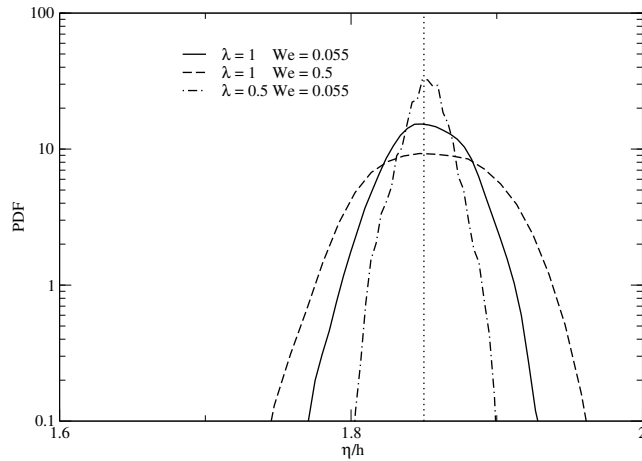


Fig. 4.7 Probability Density Function (PDF) of the interface elevation  $\eta/h$  at  $\lambda = 1$  with two different Weber number ( $We = 0.055$ ,  $We=0.5$ ) and  $\lambda = 0.5$  with  $We = 0.055$  using a logarithmic scaling. The dotted line at  $z = 1.85$  marks the reference interface position.

values. This means that crests of the interface elevation are correlated with negative fluctuations of the wall shear stress. This behaviour is in agreement with the work of Ahmadi et al. ([19]) who report a strong correlation between the crests of the interface and the shear stress inversion. The situation changes completely when  $We = 0.5$  where, consistently with the PDF of the wall shear stress fluctuations at the lubricated wall in fig.4.6, the range of the wall shear stress fluctuations is narrowed. Interestingly, in this case we do not see any flow recirculation ( $\tau'_w < -1$ ) associated with the interface deformation and this instance is happening in this case when the larger excursion around the mean position due to the lower surface tension should enhance the geometrical situation described in Ahmadi et al. ([19]).

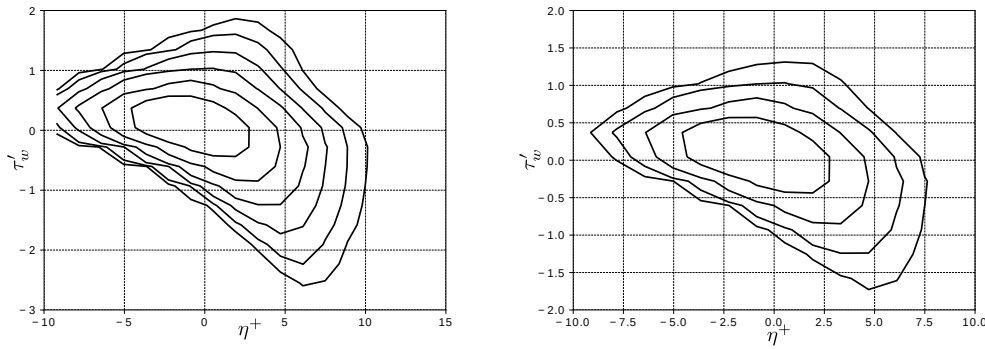


Fig. 4.8 Joint Probability Density Function (JPDF) of the normalized Wall-Shear stress fluctuations  $\tau'_w = (\tau_w - \bar{\tau})/\bar{\tau}$  over the interface elevation  $\eta^+$  in viscous units for increasing *Weber* number at  $\lambda = 1$ .

### 4.3 Turbulent kinetic energy budgets

Lastly, we examine the Turbulent Kinetic Energy (TKE) budget. The equation of the TKE for the two-fluid case, considering the symmetries of the channel flow at statistically steady state, can be written as

$$-\overline{u'w'}\frac{d\bar{u}}{dz} = -\frac{1}{2}\frac{d}{dz}\overline{u'_i u'_i w'} + \frac{d}{dz}\overline{u'_i T'_{i3}} \quad (4.4)$$

$$-\frac{1}{\rho}\frac{d}{dz}\overline{p'w'} - \epsilon + \psi_\sigma.$$

In the equation above we have production on the left-hand side and turbulent convection, viscous diffusion, pressure transport, dissipation  $\epsilon = \overline{T'_{ij} \frac{\partial}{\partial x_j} u'_i}$  and the contribution due to the surface tension  $\psi_\sigma = \frac{1}{We} \overline{u'_j f'_{\sigma,j}}$  on the right-hand side.

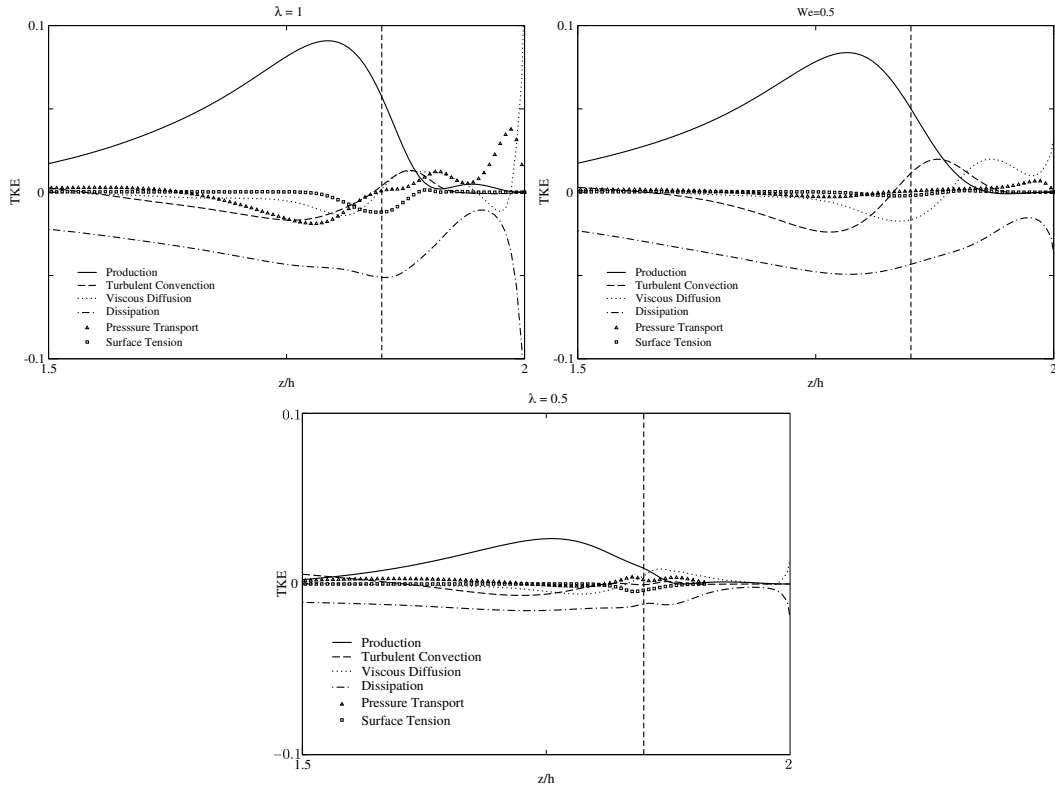


Fig. 4.9 Profiles of the contributions to the TKE budget near the lubricated wall region for the cases  $\lambda = 1$  (top left  $We = 0.0055$  and right panel  $We = 0.5$ , respectively) and for  $\lambda = 0.5$  bottom panel.

Profiles of the various component of the TKE budget for the three simulations are reported in Fig.4.9. The contributions at the non lubricated wall normalized considering the friction velocity related to the thicker fluid does not present any significant deviation from the standard well known trends for the single

phase turbulent channel flow, for this reason we did not report the plots of those profiles. In Fig. 4.9 we report instead the various terms of the equation (4.4) close to the lubricated wall normalized by  $u_\tau^4/\nu$ . We start analyzing the cases where two fluids have equal viscosity i.e.  $\lambda = 1$  (top right and left panels of Fig.4.9). Similarly to classical turbulent channel flow, in the bulk only dissipation and production present a significant contribution to the balance. Approaching the interface for increasing values of the wall-normal direction, production starts to decrease. In both cases (but also for the lower viscosity case that we will discuss later) the peak of the production has been moved far away from the lubricated wall, suggesting that the turbulence is sustained by fluctuations occurring in the non lubricating layer but close to the interface. This observation is in agreement with the dynamics of vorticity discussed in Fig.4.5. As expected, in correspondence of the maximum of production we observe negative values of convection, diffusion and pressure terms which are related with the redistribution of the turbulence kinetic energy via these three processes starting from the production layer.

Looking at the surface tension term we observe that its value is substantially negative, reaching its lowest value in the vicinity of the interface. This result suggests that the effect of the interface in energetic terms is that of a sink. Comparing the two results at  $\lambda = 1$  we can try to infer the role of the interface dynamics. Our results suggest that even if in the case with larger  $We$  the interface excursion is larger, its explicit dynamic role is mostly controlled by the surface tension that is one order of magnitude larger for the case shown in the top left panel of Fig. 4.9. It is worth mentioning that even if, according to our data, the magnitude of the contribution of the surface tension on the TKE budget is very small compared to the previous study by Zonta et al. ([42]), we still observe the same overall effect in terms of Drag Reduction. Continuing our analysis of the various terms in the lubricating layer we report that the most of the terms become not relevant, with the exception of the pressure term

which presents a larger peak for the case at  $We = 0.0055$ .

We conclude our analysis of the turbulent kinetic energy budget looking at the case with  $\lambda = 0.5$  in the bottom panel of Fig. 4.9. As mentioned before, also in this case we observe a peak of the turbulent production in the proximity of the interface in the side far from the wall. However its numerical value is nearly halved with respect to the previous cases, consistently with the observation that a nearly complete relaminarization is occurring for this case. On the other hand, examining the term due to the surface tension we see that the value of this contribution is lower than that shown for the case without viscosity difference at the same Weber. In line with the previous discussion, it is possible to explain this result considering that the forces due to surface tension are also modulated by the deformation that we expect smaller in this case because of the absence of turbulence.

## 4.4 Single point scale energy budget

To understand the dynamic of turbulence is necessary to look into the processes that involves the transfer of energy across the various length scales of eddies [26]. An **eddy** is conceived to be a turbulent motion localized within a region of size  $L$ . Turbulence can be considered to be composed by eddies of different sizes. Largest eddies created by instabilities in the mean flow break-up and evolve into smaller vortices. There is a continuous cascade of energy from large scale down to the small. Wall-bounded turbulent flows are characterized by a mean velocity gradient which produces a strong inhomogeneity in the energy flux in the wall normal direction [26]. In this study has been considered a channel with dimensions  $L_x \times L_y \times L_z = 8h \times 4h \times 2h$ , with  $h$  the half-channel height (see fig.3.1). The computational domain is composed by  $N_x \times N_y \times N_z = 304 \times 200 \times 352$  points. The flow is periodic in the streamwise  $x$  and spanwise  $y$  directions, with no-slip conditions in the normal direction  $z$  and it is driven by

a constant pressure gradient. The velocity field is, as customary, decomposed into a mean and a fluctuating component,

$$\mathbf{u} = \mathbf{u}(\mathbf{x}) + \mathbf{u}'(\mathbf{x}, t) \quad (4.5)$$

The first tool to investigate the dynamic of the channel is given by the analysis of the Turbulent Kinetic Energy (TKE) budget described by the following equation,

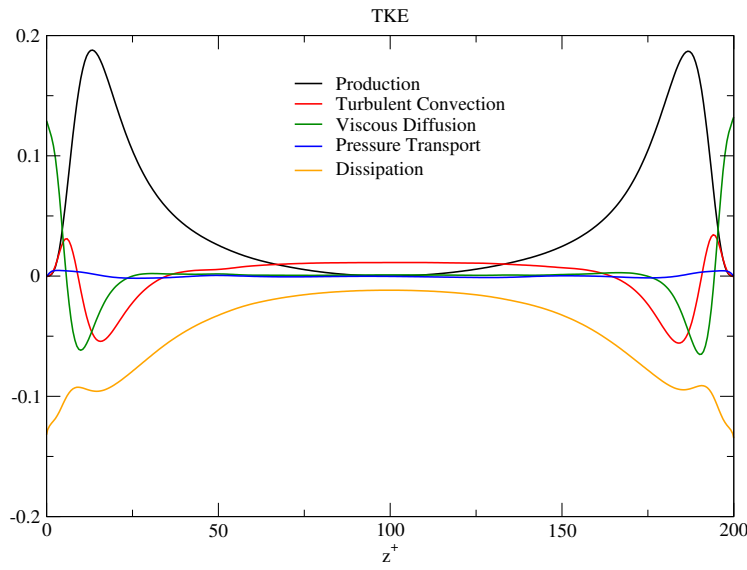


Fig. 4.10 Budget of turbulent kinetic energy (TKE) vs. wall-normal position  $z^+$  in the single-phase channel at  $Re_\tau = 100$ . Curves show: (1) production  $P(z^+)$ , (2) turbulent transport  $T(z^+)$ , (3) viscous diffusion  $D(z^+)$ , (4) pressure transport  $\Pi(z^+)$ , and (5) dissipation  $\varepsilon(z^+)$ . All terms are normalized by  $u_\tau^4/h$ . Note how production peaks in the buffer layer ( $5 < z^+ < 30$ ) and is balanced by dissipation in the log layer ( $z^+ > 30$ ), with viscous diffusion dominating very near the wall ( $z^+ < 5$ ).

$$-u'w' \frac{du}{dz} = -\frac{1}{2} \frac{d}{dz} u'_i u'_i w' + \frac{\nu}{2} \frac{d^2}{dz^2} u'_i u'_i - \frac{1}{\rho} \frac{d}{dz} p' w' - \varepsilon. \quad (4.6)$$

where respectively we have production, turbulent convection, viscous diffusion, pressure transport, pseudo-dissipation  $\varepsilon = \nu \partial u'_i / \partial x_j \partial u'_i / \partial x_j$ .

The above equation can be written in terms of the turbulent kinetic energy  $q = u'_i u'_i / 2$ ,

$$\frac{d\phi}{dz} = -u'w' \frac{du}{dz} - \epsilon, \quad (4.7)$$

where has been introduced the spatial flux  $\phi = qw' + p'w'/\rho - \nu dq/dz$ . The divergence of the flux balances with production and pseudo-dissipation [27]. The terms in the equation 4.7 allow for the identification of different regions in the flow. The first one close to the wall, dominated by dissipation, is normally referred to as the viscous sublayer ( $z^+ < 5$ ). In turn, the intermediate region where production is predominant is generally called the buffer layer ( $5 < z^+ < 30$ ). The region above, conventionally called logarithmic ( $z^+ > 30$  and  $z/h < 0.3$ ) approximately balances production with dissipation and the rate of spatial energy flux is nearly zero. The superscript + as customary implies non-dimensionalization in viscous units. In fig.4.10 profiles are all symmetrical to the center line, this represent a confirmation that the statistics has reached the steady state. At the walls the terms of diffusion and dissipation balance each other while all other terms are zero due to the boundary conditions. Around the peak of the production the flux contributes to the energy supply of regions both below and above. Through the region where the ratio between production and dissipation is approximately constant, the flux feeds the energy in the bulk region (where mean shear is negligible).

## 4.5 Two point scale energy budget

The equation 4.7 alone can not describe the full dynamic of turbulence. Different phenomena occurring in wall-bounded turbulence strongly depend not only on the geometrical space (namely the distance from the wall), but also on the range of scales. The energy associated with a specific scale of motion is transferred both to other scales and across region of shear. It is necessary a description based on the physical space and the space of scales to address the dynamic of wall-bounded turbulence. The theoretical framework that combined

these approaches is represented by the Kolmogorov equation, which assuming **homogeneity** and **isotropy** describes the transfer of energy among scales,

$$\frac{\partial \delta q \delta u'_i}{\partial r_i} = -4\epsilon + 2\nu \frac{\partial}{\partial r_i} \left( \frac{\partial \delta q}{\partial r_i} \right) \quad (4.8)$$

where  $\delta q = \delta u'^2 = \delta u'_i \delta u'_i$  is the second order structure function,  $\delta u'_i = u'_i(x_s + r_s) - u'_i(x_s)$  the fluctuating velocity increment and  $\mathbf{r} = (r_x, r_y, r_z)$  separation vector [28]. It is customary refer to  $\delta u'^2$  as a scale energy inasmuch it represents the amount of fluctuation energy at scale  $r = \sqrt{r_s r_s}$ . In the inertial range where the viscous effects are negligible, the energy flux is balanced by the energy dissipation. Approaching the viscous sublayer instead, the dissipation is balanced by the viscous diffusion while the inertial term vanishes. In wall turbulence inhomogeneous and anisotropic flows affect all relevant processes in various ranges of scales that may vary appreciably in the different flow regions. Those effects extend up to the smallest scales where even a reverse energy cascade occurs [28–30]. The extension of the Kolmogorov Equation to inhomogeneous condition in the augmented space  $(r_x, r_y, r_z, z_c)$  can be written as

$$\begin{aligned} & \frac{\partial \delta q \delta u'_i}{\partial r_i} + \frac{\partial \delta q \delta \bar{u}}{\partial r_x} - 2\nu \frac{\partial}{\partial r_i} \left( \frac{\partial \delta q}{\partial r_i} \right) + \frac{\partial w'^* \delta q}{\partial z_c} + \frac{2}{\rho} \frac{\partial \delta p' \delta w'}{\partial z_c} \\ & - \frac{\nu}{2} \frac{\partial}{\partial z_c} \left( \frac{\partial \delta q}{\partial z_c} \right) = - \left( 2\delta u' \delta w' \left( \frac{d\bar{u}}{dz} \right)^* + 2w'^* \delta u \delta \left( \frac{d\bar{u}}{dz} \right) + 4\epsilon^* \right), \end{aligned} \quad (4.9)$$

where the asterisk denotes a mid-point average  $(u'_i(x_s) + u'_i(x_s + r_s))/2$  and  $z_c = (z'_s - z_s)/2$  with  $z'_s = z_s + r_s$ . This equation for  $r \gg l$ , where  $l$  is the correlation length, reduces, within a factor 4, to the single-point energy budget 4.10. Equation 4.9 can give an insight of how turbulence is generated, redistributed and dissipated through the space of scales and physical space of wall turbulence [31]. Formally the scale energy budget can be recast as

$$\nabla \cdot (\Phi_{r_i} + \Phi_{z_c}) = \xi(r_i, z_c) \quad (4.10)$$

Where the terms in the equation represent respectively

- $\Phi_{r_i}$  in the space of scales
- $\Phi_{z_c}$  in the geometrical space
- $\xi(r_i, z_c)$  is the scale energy source

We are overall considering an four-dimensional augmented space  $(r_x, r_y, r_z, z_c)$  [32]. In homogeneous conditions consistently with the classical Richardson cascade, the source term is always negative  $\xi(r) \leq 0$  [31]. The energy transfer mechanism begins at largest scales where  $\xi(\infty) = 0$ , then moves toward small scales where  $\xi(0) = -4\epsilon^*$ . In wall turbulence may occurs that at some scales the production exceeds the dissipation, namely the source term reaches positive values.

The following analysis is performed on the **hyper-planes**  $(r_x, 0, 0, z_c)$  and  $(0, r_y, 0, z_c)$  in order to investigate the energy processes at fixed wall distance.

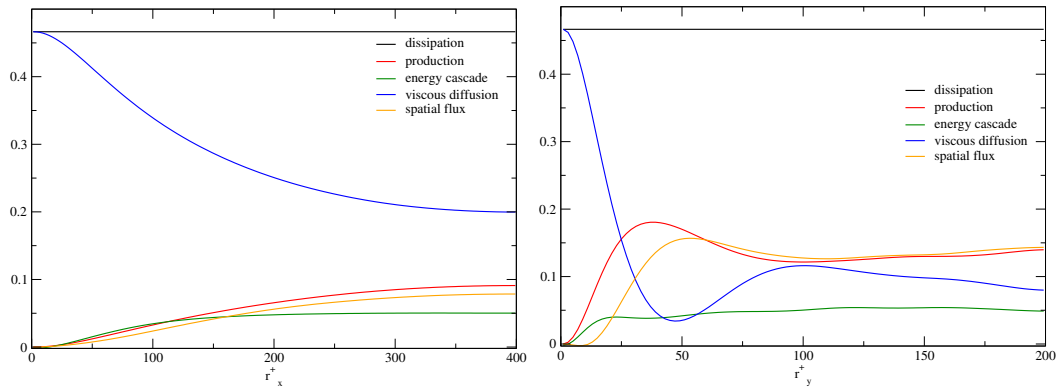


Fig. 4.11 Energy budget in the viscous sub-layer  $z^+ = 4$ ,  $(r_x^+ = 1, r_y^+ = 1)$

The first scale energy budget considered 4.11 is related to the viscous sublayer region. In the streamwise direction (left panel) all terms are very small except for the viscous diffusion. There is no significant deviation of the trends at larger scales. The picture in the spanwise direction is instead very different. Despite the proximity to the wall the profiles are in agreement with the trends at further distances. Moving towards the bulk region, in the buffer layer fig.4.12,

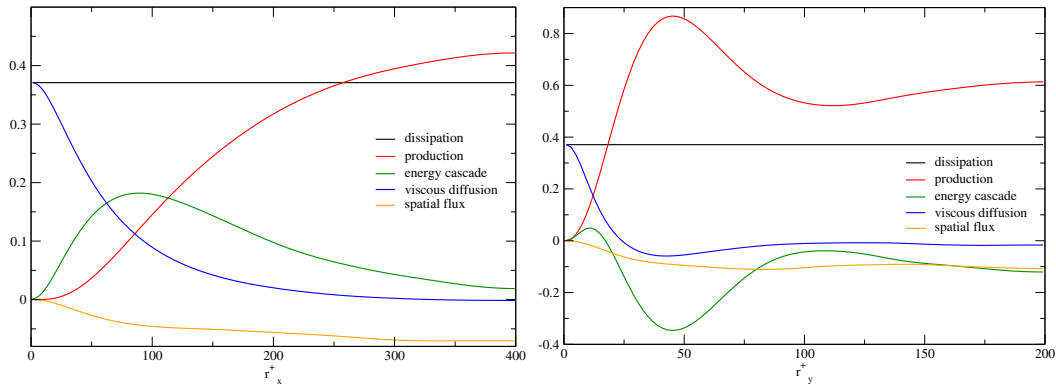


Fig. 4.12 Energy budget in the buffer layer  $z^+ = 20$ ,  $(r_x^+ = 1, r_y^+ = 1)$

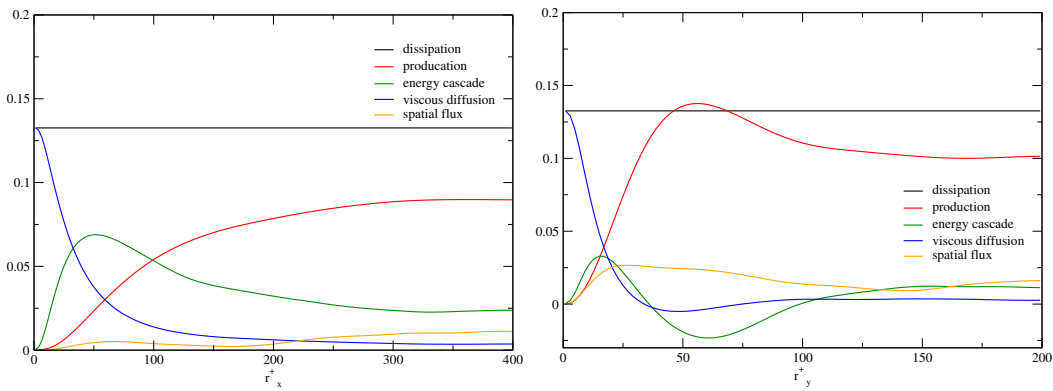


Fig. 4.13 Energy budget in the log-region  $z^+ = 50$ ,  $(r_x^+ = 1, r_y^+ = 1)$

an excess of scale energy can be seen when  $r_x^+ > 250$  in the streamwise direction. The picture reproduce, a part from the source term, the classic behavior of turbulence, where the energy is produced at large scales, then transferred to small scales and diffused by viscous forces. The strangest phenomena here occurs in the spanwise direction. As shown in the right panel of the fig.4.12 a strong peak appears at small scales for  $r_y^+ \approx 45$ . This peak produces a large reverse energy flux towards smaller and larger scales. The last energy budget 4.13 is related to the log-region. At this distance from the wall, the streamwise production occurs at large scales. The generation process is followed by the inertial energy cascade. In this region the homogeneous local conditions are fulfilled. The energy cascade rate  $\partial \delta q \delta u_i' / \partial r_i$  is always positive as expected. Instead, considering the spanwise scales of the energy budget at the same wall distance (right panel), it can be notice that the production has much higher

values at smaller scales. Furthermore for scales  $45 < r_y^+ < 70$  the production exceeds the dissipation, namely  $\xi(r) \geq 0$ . This is an unexpected result in the log-layer which is universally considered an equilibrium layer where these two quantities balance. As a consequence the positive divergence of the flux in eq.4.10 means that the inertial energy transfer feeds scales in both directions, therefore a reverse energy flux takes place.

In this chapter, we assessed the role of the interface in the mechanism of drag reduction. The main difference compared to previous studies consists in the selection of the Volume of Fluid (VoF) method for tracking the interface as an alternative approach to the Phase-Filed method. Our analysis confirmed the increase of DR when decreasing the viscosity ratio, as a result of a near complete relaminarization of the lubricated layer and a corresponding increase in the volume flow rate of 20%. On the other hand, unlike previous results, we did not observe a significant contribution of the surface tension to the turbulent kinetic energy, in terms of work spent to deform the interface. The two-point scale energy budget further explores the redistribution and energy transfer across different scales within the turbulent flow. These findings are consistent with the statistical trends presented in the preceding sections.



# Chapter 5

## Conclusions

In this work we performed a Direct Numerical Simulation of a two-phase turbulent channel flow to investigate the drag reduction associated to the presence of a thin layer of a lubricating fluid near one of the two walls. To the best of the author's knowledge this is the first study where such flow is conducted using the Volume of Fluid. We considered a configuration of the two immiscible fluids with same density. For the viscosity ratio, two different values were selected,  $\lambda = 1$  and  $\lambda = 0.5$ . For the case with same viscosity we run two simulation with different Weber number,  $We = 0.055$  and  $We = 0.5$ . Compared to the single phase case the presence of a lubricating layer strongly modify the mean statistics analyzed. In particular we observe a strong increase of the flow rate. In the case of  $\lambda = 0.5$ , a nearly complete relaminarization of the lubricated layer was observed, while the increase in the volume flow rate reached a value of 20%. Even when keeping the viscosity ratio  $\lambda = 1$ , an increase in the volume flow rate was observed, which proves that the drag reduction mechanism is already in place, with a slightly higher value when the Weber number is larger. The simulations were conducted at a relatively small shear Reynolds number,  $Re_\tau = 100$ , however the parametric analysis on the effect of viscosity ratio and surface tension allowed us to highlight very interesting modulations of the dynamics of the interface and of the turbulent kinetic budgets. Our results show some differences compared to the previous

the work of Ahmadi et al [28, 19], which can be easily traced back to the method used for the interface capturing method.

# References

- [1] Jacqmin, D. (1999). *Calculation of Two-Phase Navier-Stokes Flows Using Phase-Field Modeling*. Journal of Computational Physics. <https://doi.org/10.1006/jcph.1999.6332>
- [2] Tryggvason, G., Scardovelli, R., & Zaleski, S. (2011). *Direct numerical simulations of Gas-Liquid multiphase flows*. In *Direct Numerical Simulations of Gas-liquid Multiphase Flows*. <https://doi.org/10.1017/CBO9780511975264>
- [3] Prandtl, L. (1925). *Bericht über Untersuchungen zur ausgebildeten Turbulenz*. Zeitschrift für Angewandte Mathematik und Mechanik, 5(2), 136–139.
- [4] von Kármán, T. (1930). *Mechanische Ähnlichkeit und Turbulenz*. Nachrichten der Königlichen Gesellschaft der Wissenschaften zu Göttingen, Mathematisch-Physikalische Klasse, 58–76.
- [5] Sussman, P., & Puckett, E. G. (2000). *A coupled level set and volume-of-fluid method for computing 3D and axisymmetric incompressible two-phase flows*. Journal of Computational Physics, 162(2), 301–337. <https://doi.org/10.1006/jcph.2000.6519>
- [6] Unverdi, S. O., & Tryggvason, G. (1992). *A front-tracking method for viscous, incompressible, multi-fluid flows*. Journal of Computational Physics, 100(1), 25–37. [https://doi.org/10.1016/0021-9991\(92\)90240-F](https://doi.org/10.1016/0021-9991(92)90240-F)

- 
- [7] Bai, R., Chen, K., & Joseph, D. D. (1992). *Lubricated pipelining: Stability of core—annular flow. Part 5. Experiments and comparison with theory.* *Journal of Fluid Mechanics*. <https://doi.org/10.1017/S0022112092000041>
- [8] Chen, K., Bai, R., & Joseph, D. D. (1990). *Lubricated pipelining. Part 3 Stability of core-annular flow in vertical pipes.* *Journal of Fluid Mechanics*. <https://doi.org/10.1017/S0022112090000131>
- [9] Renardy, Y. (1984). *Instability of the flow of two immiscible liquids with different viscosities in a pipe.* *Journal of Fluid Mechanics*. <https://doi.org/10.1017/S0022112084000860>
- [10] Kouris, C., & Tsamopoulos, J. (2001). *Dynamics of axisymmetric core-annular flow in a straight tube. I. The more viscous fluid in the core, bamboo waves.* *Physics of Fluids*. <https://doi.org/10.1063/1.1352623>
- [11] Prosperetti, A., & Tryggvason, G. (Eds.). (2009). *Computational Methods for Multiphase Flow*. Cambridge University Press. <https://doi.org/10.1017/CBO9780511598946>
- [12] Debarre, R. (1974). *A piecewise linear interface calculation (PLIC) scheme for two-phase flows.* *Journal of Computational Physics*. [https://doi.org/10.1016/0021-9991\(74\)90010-5](https://doi.org/10.1016/0021-9991(74)90010-5)
- [13] Sussman, P., Smereka, P., & Osher, S. (1994). *A level set approach for computing solutions to incompressible two-phase flows.* *Journal of Computational Physics*, 114(1), 146–159. <https://doi.org/10.1006/jcph.1994.1155>
- [14] Enright, D., Fedkiw, R., Ferziger, J., & Mitchell, I. (2002). *A hybrid particle level set method for improved interface capturing.* *Journal of Computational Physics*, 183(1), 83–116. <https://doi.org/10.1006/jcph.2002.7165>

- [15] Popinet, S. (2009). *An accurate adaptive solver for surface tension driven interfacial flows*. Journal of Computational Physics, 228(16), 5838–5866. <https://doi.org/10.1016/j.jcp.2009.04.042>
- [16] Olsson, E., & Kreiss, G. (2005). *A conservative level set method for two-phase flows*. Journal of Computational Physics, 210(1), 225–246. <https://doi.org/10.1016/j.jcp.2005.01.017>
- [17] Govindarajan, R., & Sahu, K. C. (2014). *Instabilities in viscosity-stratified flow*. *Annual Review of Fluid Mechanics*. <https://doi.org/10.1146/annurev-fluid-010313-141351>
- [18] Ahmadi, S., Roccon, A., Zonta, F., & Soldati, A. (2018). *Turbulent Drag Reduction by a Near Wall Surface Tension Active Interface*. Flow, Turbulence and Combustion. <https://doi.org/10.1007/s10494-018-9918-2>
- [19] Ahmadi, S., Roccon, A., Zonta, F., & Soldati, A. (2018). *Turbulent drag reduction in channel flow with viscosity stratified fluids*. Computers and Fluids. <https://doi.org/10.1016/j.compfluid.2016.11.007>
- [20] Roccon, A., Zonta, F., & Soldati, A. (2021). *Energy balance in lubricated drag-reduced turbulent channel flow*. Journal of Fluid Mechanics. <https://doi.org/10.1017/jfm.2020.1059>
- [21] Esposito, M. C., Scapin N, Andreas D. Demou, Rosti, E., Costa, P., Spiga, F., Brandt, L. (2022), *FluTAS: A GPU-accelerated finite difference code for multiphase flows*. <https://doi.org/10.1016/j.ijmultiphaseflow.2019.04.019>
- [22] Ii, S., Sugiyama, K., Takeuchi, S., Takagi, S., Matsumoto, Y., & Xiao, F. (2012). *An interface capturing method with a continuous function: The THINC method with multi-dimensional reconstruction*. Journal of Computational Physics. <https://doi.org/10.1016/j.jcp.2011.11.038>

- 
- [23] Rosti, M. E., De Vita, F., & Brandt, L. (2019). *Numerical simulations of emulsions in shear flows*. Acta Mechanica. <https://doi.org/10.1007/s00707-018-2265-5>
- [24] Mirjalili, S., Ivey, C. B., & Mani, A. (2019). *Comparison between the diffuse interface and volume of fluid methods for simulating two-phase flows*. International Journal of Multiphase Flow. <https://doi.org/10.1016/j.ijmultiphaseflow.2019.04.019>
- [25] Kim, J., Moin, P. Moser, R. (1987). *Turbulence statistics in fully developed channel flow at low reynolds number*. Journal of Fluid Mechanics. <https://doi.org/10.1017/S0022112087000892>
- [26] Saikrishnan, N., De Angelis, E., Longmire, E. K., Marusic, I., Casciola, C. M., & Piva, R. (2012). *Reynolds number effects on scale energy balance in wall turbulence*. Physics of Fluids. <https://doi.org/10.1063/1.3673609>
- [27] Cimarelli, A., & De Angelis, E. (2011). *Analysis of the Kolmogorov equation for filtered wall-turbulent flows*. Journal of Fluid Mechanics. <https://doi.org/10.1017/S0022112011000565>
- [28] Marati, N., Casciola, C. M., & Piva, R. (2004). *Energy cascade and spatial fluxes in wall turbulence*. Journal of Fluid Mechanics. <https://doi.org/10.1017/S0022112004001818>
- [29] Piomelli, U., Yu, Y., & Adrian, R. J. (1996). *Subgrid-scale energy transfer and near-wall turbulence structure*. Physics of Fluids. <https://doi.org/10.1063/1.868829>
- [30] Dunn, D. C., & Morrison, J. F. (2003). *Anisotropy and energy flux in wall turbulence*. Journal of Fluid Mechanics. <https://doi.org/10.1017/S0022112003005548>

- [31] Cimarelli, A., & De Angelis, E. (2012). *Anisotropic dynamics and sub-grid energy transfer in wall-turbulence*. *Physics of Fluids*. <https://doi.org/10.1063/1.3675626>
- [32] Cimarelli, A., De Angelis, E., & Casciola, C. M. (2013). *Paths of energy in turbulent channel flows*. *Journal of Fluid Mechanics*. <https://doi.org/10.1017/jfm.2012.528>
- [33] Jacqmin, D. (1999). *Calculation of Two-Phase Navier-Stokes Flows Using Phase-Field Modeling*. *Journal of Computational Physics*. <https://doi.org/10.1006/jcph.1999.6332>
- [34] Soligo, G., Roccon, A., & Soldati, A. (2019). *Coalescence of surfactant-laden drops by Phase Field Method*. *Journal of Computational Physics*. <https://doi.org/10.1016/j.jcp.2018.10.021>
- [35] Roccon, A., Zonta, F., & Soldati, A. (2019). *Turbulent drag reduction by compliant lubricating layer*. *Journal of Fluid Mechanics*. <https://doi.org/10.1017/jfm.2019.8>
- [36] Roccon, A., Zonta, F., & Soldati, A. (2021). *Energy balance in lubricated drag-reduced turbulent channel flow*. *Journal of Fluid Mechanics*. <https://doi.org/10.1017/jfm.2020.1059>
- [37] Van Kan, J. (1986). *A second-order accurate pressure-correction scheme for viscous incompressible flow*. *SIAM Journal on Scientific and Statistical Computing*, 7(3), 870–891. <https://doi.org/10.1137/0907059>
- [38] Harlow, F. H., & Welch, J. E. (1965). *Numerical calculation of time-dependent viscous incompressible flow of fluid with free surface*. *Physics of Fluids*, 8(12), 2182–2189. <https://doi.org/10.1063/1.1761178>
- [39] Ii, S., Sugiyama, K., Takeuchi, S., Takagi, S., Matsumoto, Y., & Xiao, F. (2012). *An interface capturing method with a continuous function:*

- 
- The THINC method with multi-dimensional reconstruction.* Journal of Computational Physics. <https://doi.org/10.1016/j.jcp.2011.11.038>
- [40] Rosti, M. E., De Vita, F., & Brandt, L. (2019). *Numerical simulations of emulsions in shear flows.* Acta Mechanica. <https://doi.org/10.1007/s00707-018-2265-5>
- [41] Mirjalili, S., Jain, S. S., & Dodd, M. S. (2017). *Interface capturing methods for two-phase flows: An overview and recent developments.* Center for Turbulence Research: Annual Research Briefs
- [42] Mirjalili, S., Ivey, C. B., & Mani, A. (2019). *Comparison between the diffuse interface and volume of fluid methods for simulating two-phase flows.* International Journal of Multiphase Flow. <https://doi.org/10.1016/j.ijmultiphaseflow.2019.04.019>